Virtual laboratory enabled constitutive modelling of dual phase steels

Wencheng Liu [a], Xinghao Li [a], Ming Liu [c], Hao Cui [a], Jia Huang [a], Yong Pang [d], Jun Ma [b,*]

[a] School of Civil Aviation, Northwestern Polytechnical University, Xi'an 710072, China
[b] Department of Mechanical and Industrial Engineering, Norwegian University of Science and Technology, Trondheim 7491, Norway
[c] State Key Laboratory of Electromechanical Integrated Manufacturing of High-performance Electronic Equipments, Xidian University, Xi'an 710071, China
[d] School of Engineering and Materials Science, Queen Mary University of London, London E1 4NS, UK

ARTICLE INFO

ABSTRACT

Accurate and efficient characterization and modelling of deformation responses are critically essential in the development of advanced metal forming processes. This work presents a virtual laboratory enabled constitutive framework for modelling complex deformation responses of dual phase (DP) steels under complex stress states, based on multi-phase full-field crystal plasticity (CP) and advanced phenomenological modelling. In the CP based virtual testing method, kinematic hardening and degradation of elastic modulus are modelled in particular to improve the capability for describing evolving microstructure induced mechanical responses of DP steels. The workflow of this framework is completely built and numerically implemented, including (i) representative volume element (RVE) generation based on microstructure characterization, (ii) identification of multiphase CP model parameters, (iii) prediction of elastic modulus degradation, (iv) prediction of yield stresses and plastic potentials in uniaxial tension and biaxial tension with various stress ratios, and (v) prediction of stress–strain curves in reverse tension compression. Using DP780 and DP980 as case materials, the corresponding physical experiments are conducted to verify the accuracy of the virtual tests, showing a good agreement between the virtual and experimental approaches. Both experimental and virtual tests are used to calibrate advanced phenomenological constitutive models that include non-linear elasticity, anisotropic yielding, and kinematic hardening. The calibrated models are implemented into the finite element (FE) codes to predict complex deformation and springback behaviours of DP780 and DP980 sheets in U-bending processes. In comparison with forming experiments of U-channel parts, the virtually calibrated models are validated and show good performance in predicting deformation and springback behaviours, providing a high capability for process analysis. The findings support that the virtual laboratory enabled modelling approach could be a substitute for extensive, expensive, and hard-to-access physically mechanical experiments required in the model calibration for a more effective and efficient analysis of metal forming processes.

1. Introduction

The demand for lightweight automotive structure design has increased significantly in the electric vehicle (EV) industry to increase the driving range. Advanced metallic materials such as advanced high-strength steel (AHSS) and high-strength aluminium

alloy are increasingly used to fabricate components of automotive structures due to their high strength-to-weight ratios and excellent overall performance (Zhang and Xu, 2022; Welo et al., 2020). Dual-phase (DP) steels, a typical type of AHSS with good formability, are greatly favoured in manufacturing automotive structures. The microstructure of dual-phase steel is characterized by a mixture of two phases with different crystal arrangements — the first is the soft and ductile ferrite phase, while the second is the hard and brittle martensite phase. The presence of the martensite phase enables DP steels to have a higher strength and hardness, while the soft ferrite phase provides excellent ductility and formability. However, the high strength and complex plastic anisotropy of DP steels do exist and evolve in deformation, making it difficult to achieve high-precision forming of complex structure components; especially, the significant springback problem is still a challenge that limits the wider application of DP structures. Springback occurs at the end moment of the entire forming process, so almost all factors throughout the forming operation can affect the deformation behaviour and thus the springback (Wagoner et al., 2013). Therefore, it is essential to accurately characterize the mechanical properties and develop a reliable and cost-effective modelling approach for the accurate analysis of forming processes and springback.

By now, various phenomenological constitutive models have been proposed to predict the anisotropic plastic deformation, kinematic hardening, and unloading behaviours involved in DP steel forming processes. In terms of anisotropic yielding and hardening, Marcadet and Mohr (2015) investigated the hardening behaviour of DP780 steels in reverse compression–tension loading and used it to calibrate the Frederick Armstrong and a Yoshida–Uemori (YU) type model (Yoshida and Uemori, 2002; Chaboche, 2008). Hou et al. experimentally investigated the evolution of the yield surface during the uniaxial tensile tests and biaxial tensile tests for three types of DP steels with various phase volume fractions. These data were utilized to calibrate various advanced yield functions (Hou et al., 2019, 2021). The shear tension–compression tests were conducted by Min et al. (2021) for DP980 steel to calibrate the YU kinematic hardening model, which indicates that YU models are capable of accurately predicting the springback of DP980 steel. Hérault et al. proposed a constitutive model for DP600 steel by combining the Yld2000-2d yield function and the enhanced homogeneous anisotropic hardening (e-HAH) model (Barlat et al., 2013, 2014) to describe the initial plastic anisotropy and its evolution with change of strain path, respectively (Hérault et al., 2021). The latest HAH_{20} model proposed by Shin-Yeong Lee et al. show a good performance in the prediction of springback of high-strength steels in U-draw bending (Lee et al., 2023). In this work, the experimental mechanical behaviour of DP steels under different strain paths and strain ranges was successfully captured by this model. In terms of deformation-induced elastic modulus degradation, Xue et al. experimentally investigated the variation of the elastic modulus of DP steels in various prestrain levels under uniaxial and biaxial tensions. These data were utilized to calibrate the Yld2000-2d yield function (Barlat et al., 2003) associated with the chord elastic model (Yoshida et al., 2002), which was used to perform springback prediction after DP steels forming (Xue et al., 2016a). The non-linear elastic behaviour of DP steels significantly affects the accuracy of springback prediction (Deng et al., 2018; Deng and Korkolis, 2018). Later, the experimentally calibrated constitutive model based on the combination of the Yld2000-2d, e-HAH and Yoshida chord modulus model was implemented in the FE code and used to predict the twist springback in the DP500 steel channel parts by Liao et al. (2017). This work takes into account elastic modulus degradation, plastic anisotropy, and kinematic hardening behaviours of DP steels, accurately predicting the springback in the forming of complicated structures. Xue et al. studied the effect of different yield functions, including von Mises, Hill48, and Yld2000-2d models associated with isotropic hardening (IH) or mixed hardening models on the accuracy of twist springback in DP500 steels channel forming (Xue et al., 2016b, 2017). The results showed that the accuracy of twist springback prediction is sensitive to the plastic anisotropy calibrated by the yield functions. Choi et al. applied various mechanical tests calibrated constitutive models constructed by the combination of Hill48 or Yld2000-2d yield function associated with YU model or HAH model to predict the springback of DP980 in U-draw bending, studying the effect of anisotropic hardening on the springback of high-strength DP steels under non-proportional loading (Choi et al., 2018). In addition, the twist springback in channel forming of DP980 was studied by Choi et al. using the Yld2000-2d yield function associated with various hardening models, including the IH model, YU model, and HAH model. The HAH model showed superior performance than the IH and YU models with respect to the prediction of twist angle after springback (Choi et al., 2016). In summary, to obtain an accurate prediction of deformation and springback in the DP steel forming of complicated structures, the constitutive models must take into account elastic modulus degradation, plastic anisotropy, and kinematic hardening behaviour. However, this kind of model generally requires extensive and costly mechanical test data, including directional uniaxial yield stress and r-value, biaxial yield locus and plastic potentials, stress–strain curves during reverse tension–compression loading, and variable elastic modulus with various prestrain levels. Additionally, these mechanical tests require expensive, specialized equipment and setups, which are not accessible in many cases, making it difficult to user-friendly calibrate the advanced constitutive models and thus limit their applications.

To further investigate the deformation behaviour of DP steels, microstructure-based modelling has been proposed to predict plastic anisotropy, hardening behaviour, and nonlinear unloading under complex strain paths (Bong et al., 2017; Ha et al., 2017; Fansi et al., 2013; Balan et al., 2015; Poulin et al., 2019; Park et al., 2021; Daroju et al., 2022). The mechanical properties of DP steels at the grain-length scale are significantly influenced by microstructure features such as martensite and ferrite phase volume fraction, crystalline morphology, the interface of the phase boundary, and crystalline texture (Soliman and Palkowski, 2020; Tian et al., 2020; Li et al., 2019; Liu et al., 2019b; Ebrahimi et al., 2020). At present, mean-field and full-field crystal plasticity modelling have been developed to taking these microstructural characteristics into account. For example, the mean-field crystal plasticity model using dislocation-density-based hardening model successfully predict the springback of Zr and low-carbon steel subjected to bending and unloading (Jeong et al., 2021), the amount of springback of AA6022-T4 sheets after deep-drawing (Barrett and Knezevic, 2019) and springback of EDDQ steel after 3-point-bending (Joo et al., 2023). Moreover, the HAH model is successfully incorporated into the mean-field crystal plasticity model and show a good performance in the prediction of flow stress behaviour of steels under various loading conditions (Jeong et al., 2017; Kim et al., 2018). The mean-field crystal plasticity models incorporate with dislocation-density hardening models can be applied directly to simulate the forming process and the reversal (Feng et al.,

2020). Amirmaleki et al. investigated the influence of the phase distribution and volume fraction on the stress–strain curve using the representative 3D volume element and the full-field dislocation density model (Amirmaleki et al., 2016). Zecevic et al. developed a dislocation-based crystal plasticity model for DP590 steel, which shows good performance in predicting hardening behaviour in cyclic tension–compression loading (Zecevic et al., 2016). Full-field crystal plasticity modelling, in which the crystal aggregate is discretized as a set of integration points using FE method (Kraska et al., 2009; Roters et al., 2010; Bong and Lee, 2021; Shi et al., 2022; Bong et al., 2019a) or Fourier points using FFT based spectral methods (Eisenlohr et al., 2013; Shanthraj et al., 2015; Roters et al., 2019), is widely applied to predict the plastic anisotropy and kinematic hardening of polycrystal materials (Zhang et al., 2015; Liu et al., 2020a, 2019a; Esmaeilpour et al., 2018; Liu et al., 2021). Since full-field CP modelling can describe the micromechanical behaviour for different phases using independent constitutive models, it can also be used to predict the plastic anisotropy and strain hardening of multi-phase materials. For instance, Diehl et al. proposed a full-field CP model based on 3D EBSD data to simulate the strain and stress distribution among the ferritic and martensitic phases of DP steel (Diehl et al., 2017). A dislocation-based full-field CP modelling associated with high-resolution RVEs at grain-length scale successfully predicted the effective elastic modulus, Poisson's ratio, and stress–strain curves in tension–compression loading of DP590, DP980, and DP1180 (Eghtesad and Knezevic, 2020). Ravi et al. proposed a multi-phase full-field CP model for Duplex steel consisting of Austenitic and Ferritic phases, which could be used to predict the macroscopic anisotropic yield locus (Ravi et al., 2019). Yalçinkaya et al. investigated the influence of crystal morphology on the accuracy of full-field CP modelling with respect to the prediction of stress–strain curve under uniaxial tensile loading (Yalçinkaya et al., 2021). Liu et al. studied the microscale ductile fracture behaviour of DP steel under bending using full-field CP modelling (Liu et al., 2020b). Liu et al. proposed a synthetic microstructure generation strategy and crystal plasticity parameters identification approach for dual-phase steel and investigated the effects of various microstructure features like phase fraction, grain size, grain shape, misorientation, and texture on crystal plasticity simulations (Liu et al., 2020c). Kim et al. proposed a full-field crystal plasticity model that could be utilized to predict the Bauschinger effect in cyclic loading in DP steels (Kim et al., 2012). Recently, full-field CP modelling has been utilized to perform virtual tests, which provide extensive plastic anisotropic data for the identification of advanced yield function and kinematic hardening model (Zhang et al., 2016; Gawad et al., 2015; Bong et al., 2019b; Liu, 2021; Liu et al., 2023; Yang et al., 2022; Feng et al., 2022; Xu et al., 2023; Tang et al., 2023; Marie et al., 2022). Li et al. employed full-field CP modelling-based virtual tests to study the plastic anisotropy in terms of the directional uniaxial normalized yield stress and r-value of DP980 (Li et al., 2020). Additionally, Ma et al. applied virtual tests to predict the yield locus and calibrate the parameters of the yield function in DP980 (Ma et al., 2022). In terms of unloading behaviour, Cantara et al. studied anisotropic elastic modulus based on the texture information of DP590, DP980, and DP1180 utilizing the crystal mechanics-based mean-field self-consistent homogenization approach, which is useful for investigating springback in forming processes (Cantara et al., 2019). Despite the successful development and application of full-field CP models for dual-phase steels, it is noticeable that these works mainly focus on studying micromechanical behaviour, plastic anisotropy, and strain hardening in specific loading paths. However, regarding the multi-phase full-field CP-based constitutive modelling approach for the through-process analysis from complex forming history to the final springback, relatively fewer studies refer to this critical problem. In particular, how to take the unique microstructural evolution into the multiscale modelling, thus enabling substituting the conventional phenomenological modelling approach, which highly depends on expensive physical experiments.

To address the research gap identified above, this study aims to develop a virtual laboratory based constitutive modelling framework for metal forming with high-strength DP steels. The framework employs multi-phase full-field CP modelling as a virtual laboratory to calibrate advanced phenomenological models including anisotropic yielding, kinematic hardening, and nonlinear unloading. The microstructural information of the DP steels, including the volume fraction, texture, and crystal morphology, is characterized by electron backscatter diffraction (EBSD). High-resolution multiphase RVEs are created by using microstructure information and further used to virtually test the directional uniaxial yield stresses, r-values, and biaxial yield loci. A series of mechanical tests including biaxial tension tests with various strain ratios are performed to verify the accuracy of virtual tests. Finally, the virtually calibrated constitutive models are applied and confirmed in the simulation of the U-bending processes of DP780 and DP980 steels, with a particular focus on springback analysis.

2. Virtual laboratory enabled multiscale modelling

In the conventional approach, to accurately describe the mechanical behaviour of sheet metal in the forming process, extensive mechanical tests are required to calibrate the parameters of the phenomenological constitutive models as illustrated in Fig. 1a. However, these mechanical tests generally require expensive test equipment and complicated experimental processes. With the development of a physically-based CP model, the mechanical behaviour of multi-phase materials in various loading conditions could be accurately predicted using the microstructure information of materials. This enables the CP simulations-based virtual laboratory to become a powerful approach to calibrating phenomenological constitutive models (Zhang et al., 2016). Here, a virtual laboratory based on the multi-phase full-field crystal plasticity modelling with physically-based mixed isotropic and kinematic hardening law is established for the DP steels as illustrated in Fig. 1b. It should be noted, that, by only using one group of parameters for ferrite and martensite phases calibrated by the mechanical data of uniaxial tension–compression tests, this virtual laboratory is capable of predicting the variation of elastic modulus, kinematic hardening and plastic anisotropy in various loading condition of different DP steels required by the calibration of the advanced constitutive models. In this work, both the conventional experiments and the novel virtual laboratory based constitutive modelling in sheet metal forming of the DP steels are conducted. The results of the virtual laboratory are carefully verified by the results of experimental tests including the variation of elastic modules in uniaxial
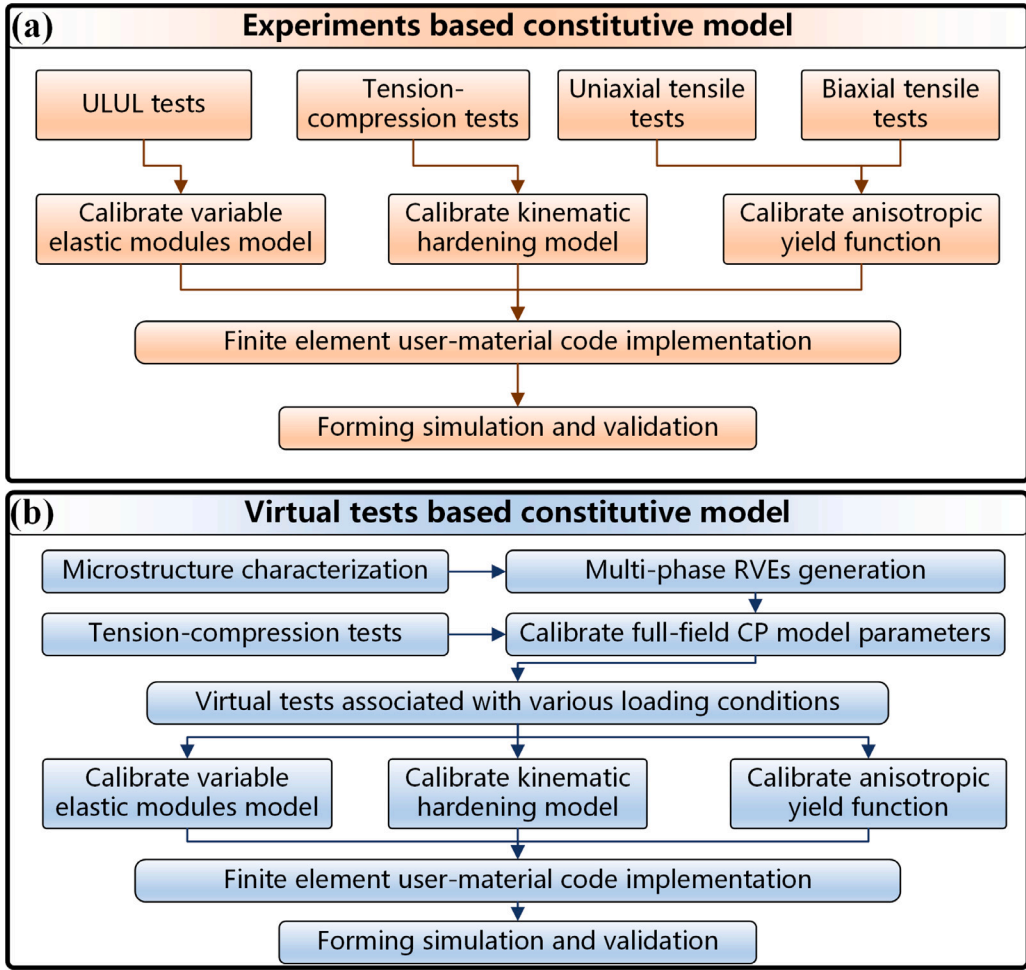
Fig. 1. (a) The flowchart of the conventional modelling approach for sheet metal forming based on extensive experimental mechanical tests. (b) The flowchart of the novel virtual laboratory enabled multi-scale modelling framework based on multi-phase full-field crystal plasticity modelling.

loading-unloading-loading (ULUL) cycle tensile test, kinematic hardening behaviours in reverse tension–compression tests and plastic anisotropy in uniaxial and biaxial tensile tests.

The constitutive formulations of the crystal plasticity model, phenomenological non-linear elastic model, yield function and kinematic hardening model are introduced in the following section to explain the physical meaning and definition of the material constants used in this work.

2.1. Crystal plasticity modelling with physically-based mixed isotropic and kinematic hardening considered

The hardening behaviour in DP steels generally show more isotropic hardening and backstress evolution in cyclic loading due to the forest dislocations and dislocation pile-up. The crystal plasticity model associated with a phenomenological mixed isotropic and kinematic hardening law on each slip system is used to predict the strain hardening behaviour of DP steels in complex loading scenarios with cyclic tension–compression loading involved (Wollmershauser et al., 2012). Here, the stress rate in a crystal c is donated as $\dot{\boldsymbol{\sigma}}^c$ is related to elastic strain rate using the small strain assumption:

$$\dot{\boldsymbol{\sigma}}^c = \mathbb{C} : \left(\dot{\boldsymbol{\varepsilon}}^c - \sum_{\alpha}^{N} \dot{\gamma}^{\alpha} \mathbf{S}_0^{\alpha} \right) \tag{1}$$

where the elastic strain rate is determined by the difference between the total strain rate $\dot{\varepsilon}^c$ and the plastic strain rate. $\dot{\gamma}^{\alpha}$ is the shear strain rate on slip system α. The Schmid tensor is obtained through the dyadic product of the unit vectors and slip plane normal directions $\mathbf{S}_0^{\alpha} = \mathbf{s}_0^{\alpha} \otimes \mathbf{m}_0^{\alpha}$. The elastic stiffness tensor, denoted by $\mathbb{C}$, pertains to the sample coordinate system. For a cubic crystal, $\mathbb{C}$ can be fully defined with reference to the crystal axis by three specific material constants, namely C_{11}, C_{12} and C_{44}.

To capture the isotropic and kinematic hardening in a single crystal, the yield criterion including an explicit backstress τ_{bs}^s for each slip system is given by,

$$\tau^s = \mathbf{S}_0^\alpha : \sigma^c - \tau_{bs}^s \tag{2}$$

where τ^s is the critical resolved shear stress (CRSS) of each slip system, which is governed by the evolution of the flow stress σ^c and backstress τ_{bs}^s. The initial value τ_0^s of the τ^s is used to phenomenologically describe the initial CRSS, which physically results from the initial density of forest dislocations, intrinsic lattice resistance, solid solution alloying, and particle strengthening at micro-scale.

The backstress τ_{bs}^s is used to describe the kinematic hardening behaviour in cyclic loading, which physically results from the increasing of the local stresses due to the GND accumulated at hard particles and grain boundary. To solve Eq. (2), its phenomenological rate equation is given by,

$$\dot{\tau}^s = \mathbf{S}_0^\alpha : \dot{\sigma}^c - \dot{\tau}_{bs}^s \tag{3}$$

The evolution of the CRSS rate is related to the shear strain rate and given by,

$$\dot{\tau}^s = \sum_\beta^N \frac{\partial \tau^s}{\partial \Gamma} h^{\alpha\beta} \dot{\gamma}^\beta \tag{4}$$

where the $h^{\alpha\beta}$ is the latent hardening matrix between the various slip systems. $\Gamma = \sum_\alpha^N \gamma^\alpha$ is the total plastic shear strain. The non-linear evolution of the backstress $\frac{\partial \tau^s}{\partial \Gamma}$ is described by an extended Voce hardening law,

$$\frac{\partial \tau^s}{\partial \Gamma} = \theta_1 + \left\{ \theta_0 - \theta_1 + \frac{\theta_0 \theta_1}{\tau_1}(\Gamma) \right\} \exp\left\{ -(\Gamma)\frac{\theta_0}{\tau_1} \right\} \tag{5}$$

where the θ_0 and θ_1 are initial and asymptotic hardening rates of CRSS. τ_1 is the back-extrapolated stress from the terminal linear hardening region. The evolution of the backstress rate is also related to the shear strain rate and given by,

$$\dot{\tau}_{bs}^s = \sum_\beta^N \frac{\partial \tau_{bs}^s}{\partial \gamma^s} h^{\alpha\beta} \dot{\gamma}^\beta \tag{6}$$

The rate of the backstress is also determined by the extended Voce hardening equation,

$$\frac{\partial \tau_{bs}^s}{\partial \gamma^\alpha} = \theta_1^{bs} + \left\{ \theta_0^{bs} - \theta_1^{bs} + \frac{\theta_0^{bs} \theta_1^{bs}}{\tau_1^{bs} + \chi_0^\alpha}\left(\gamma^\alpha - \gamma_0^\alpha\right) \right\} \exp\left\{ -(\gamma^\alpha - \gamma_0^\alpha)\frac{\theta_0^{bs}}{\tau_1^{bs} + \chi_0^\alpha} \right\} \tag{7}$$

where the θ_0^{bs} and θ_1^{bs} are initial and asymptotic hardening rates of backstress. τ_1^{bs} is the back-extrapolated stress from the terminal linear hardening region of the backstress. γ_0^α is the memory strain in the kinematic hardening, which is equal to the total accumulated shear strain on a slip system. χ_0^α is the memory stress in the kinematic hardening, which is defined as the positive resolved backstress. The efficient spectral method using FFT is utilized as the numerical solver to perform the crystal plasticity modelling with mixed isotropic and kinematic hardening constitutive law.

2.2. Deformation-induced degradation of elastic modulus

The springback prediction in simulation is very sensitive to the elastic modulus in material models. The DP steels generally show significant degradation of elastic modulus associated with the increase of the plastic strain under uniaxial tension. Therefore, it is important to accurately describe the variation of the elastic modulus in plastic deformation for accurate prediction in springback. Here, the variation of the elastic modulus in the phenomenological model at macroscopic scale is described using a function of equivalent plastic strain ε_{ep} proposed by Yoshida and Uemori (2002) and given by,

$$E = E_0 - \left(E_0 - E_a\right)\left[1 - exp\left(-\xi \varepsilon_{ep}\right)\right] \tag{8}$$

where E_0 and E_a are the initial and saturated elastic modulus and ξ is a material constant calibrated by the evolution of elastic modulus.

2.3. Phenomenological anisotropic yield function

Due to the strong texture and complex multi-phase distribution commonly observed in cold-rolled dual-phase steel, induced plastic anisotropy must be considered in constitutive models, such as the anisotropic yield criterion. However, due to limitations in current experimental technology, only in-plane plastic anisotropy can be measured through physical tensile tests with various plane stress states. Therefore, the plane stress yield function Yld2000-2d is widely used to describe experimental data. The formulation of Yld2000-2d is based on the concept of linear transformation on the stress deviator. The effective stress $\overline{\sigma}$ in this yield function is expressed as (Barlat et al., 2003):

$$\Psi\left(\widetilde{S}', \widetilde{S}''\right) = \left[\frac{1}{2}\left(\left|\widetilde{S}_1' - \widetilde{S}_2'\right|^a + \left|2\widetilde{S}_2'' + \widetilde{S}_1''\right|^a + \left|2\widetilde{S}_1'' + \widetilde{S}_2''\right|^a\right)\right]^{1/a} = \overline{\sigma} \tag{9}$$

where a is the exponent associated with the crystal structure of the materials, which determines the shape of the yield surface. The $\widetilde{S}'$ and $\widetilde{S}''$ are the principal values of $\tilde{s}'$ and $\tilde{s}'$, which are obtained by the linear transformation of the in-plane CAUCHY stress tensor:

$$\tilde{s}' = \begin{bmatrix} 2/3 & 0 & 0 \\ -1/3 & 0 & 0 \\ 0 & -1/3 & 0 \\ 0 & 2/3 & 0 \\ 0 & 0 & 1 \end{bmatrix} \begin{bmatrix} a_1 \\ a_2 \\ a_7 \end{bmatrix} \begin{bmatrix} \sigma_{xx} \\ \sigma_{yy} \\ \sigma_{xy} \end{bmatrix}, \quad \tilde{s}'' = \frac{1}{9} \begin{bmatrix} 2 & -2 & 8 & -2 & 0 \\ 1 & -4 & -4 & 4 & 0 \\ 4 & -4 & -4 & 1 & 0 \\ -2 & 8 & 2 & -2 & 0 \\ 0 & 0 & 0 & 0 & 9 \end{bmatrix} \begin{bmatrix} a_3 \\ a_4 \\ a_5 \\ a_6 \\ a_8 \end{bmatrix} \begin{bmatrix} \sigma_{xx} \\ \sigma_{yy} \\ \sigma_{xy} \end{bmatrix} \tag{10}$$

where the eight parameters $a_i, i = 1 \sim 8$, are calibrated by the experimental plastic anisotropy, including the directional uniaxial yield stress, r-value, and biaxial yield stress.

Recently, accurate virtual tests based on high-resolution full-field crystal plasticity modelling have been developed to obtain plastic anisotropy in arbitrary loading paths. Therefore, not only in-plane but also out-of-plane plastic anisotropy can be accessed through virtual tests. To accurately capture this data, the highly flexible 3D stress yield function Yld2004-18p is adopted in this work. The effective stress $\overline{\sigma}$ defined in this function is expressed as (Barlat et al., 2005):

$$\Psi\left(\widetilde{S}', \widetilde{S}''\right) = \left|\widetilde{S}'_1 - \widetilde{S}''_1\right| + \left|\widetilde{S}'_1 - \widetilde{S}''_2\right| + \left|\widetilde{S}'_1 - \widetilde{S}''_3\right| + \left|\widetilde{S}'_2 - \widetilde{S}''_1\right| + \left|\widetilde{S}'_2 - \widetilde{S}''_2\right| + \left|\widetilde{S}'_2 - \widetilde{S}''_3\right| + \left|\widetilde{S}'_3 - \widetilde{S}''_1\right|$$
$$+ \left|\widetilde{S}'_3 - \widetilde{S}''_2\right| + \left|\widetilde{S}'_3 - \widetilde{S}''_3\right| = 4\overline{\sigma}^a \tag{11}$$

where the material constant a is generally defined by the type of crystal structure, and its high value increases the ellipsoid of the yield surface. The $\widetilde{S}'_i$ and $\widetilde{S}''_i$ ($i = 1,2,3$) are the principal values of $\tilde{s}'$ and $\tilde{s}''$, which are calculated by adopting the linear transformations on Cauchy stress deviators:

$$\tilde{s}' = \begin{bmatrix} 0 & -\alpha_1 & -\alpha_2 & 0 & 0 & 0 \\ -\alpha_3 & 0 & -\alpha_4 & 0 & 0 & 0 \\ -\alpha_5 & -\alpha_6 & 0 & 0 & 0 & 0 \\ 0 & 0 & 0 & \alpha_9 & 0 & 0 \\ 0 & 0 & 0 & 0 & \alpha_7 & 0 \\ 0 & 0 & 0 & 0 & 0 & \alpha_8 \end{bmatrix} \begin{bmatrix} 2/3 & -1/3 & -1/3 & 0 & 0 & 0 \\ -1/3 & 2/3 & -1/3 & 0 & 0 & 0 \\ -1/3 & -1/3 & 2/3 & 0 & 0 & 0 \\ 0 & 0 & 0 & 1 & 0 & 0 \\ 0 & 0 & 0 & 0 & 1 & 0 \\ 0 & 0 & 0 & 0 & 0 & 1 \end{bmatrix} \begin{bmatrix} \sigma_{xx} \\ \sigma_{yy} \\ \sigma_{zz} \\ \sigma_{xy} \\ \sigma_{yz} \\ \sigma_{zx} \end{bmatrix}, \tag{12}$$

$$\tilde{s}'' = \begin{bmatrix} 0 & -\alpha_{10} & -\alpha_{11} & 0 & 0 & 0 \\ -\alpha_{12} & 0 & -\alpha_{13} & 0 & 0 & 0 \\ -\alpha_{14} & -\alpha_{15} & 0 & 0 & 0 & 0 \\ 0 & 0 & 0 & \alpha_{18} & 0 & 0 \\ 0 & 0 & 0 & 0 & \alpha_{16} & 0 \\ 0 & 0 & 0 & 0 & 0 & \alpha_{17} \end{bmatrix} \begin{bmatrix} 2/3 & -1/3 & -1/3 & 0 & 0 & 0 \\ -1/3 & 2/3 & -1/3 & 0 & 0 & 0 \\ -1/3 & -1/3 & 2/3 & 0 & 0 & 0 \\ 0 & 0 & 0 & 1 & 0 & 0 \\ 0 & 0 & 0 & 0 & 1 & 0 \\ 0 & 0 & 0 & 0 & 0 & 1 \end{bmatrix} \begin{bmatrix} \sigma_{xx} \\ \sigma_{yy} \\ \sigma_{zz} \\ \sigma_{xy} \\ \sigma_{yz} \\ \sigma_{zx} \end{bmatrix} \tag{13}$$

where the calibration of the parameters $\alpha_i, i = 1 \sim 18$, requires extensive yield stresses and plastic potentials in various stress states. Conventionally, the experimental results of uniaxial and biaxial tensile tests are utilized as input data to calibrate in-plane anisotropy, while out-of-plane anisotropy is calibrated by the prediction of crystal plasticity modelling.

In this work, the Yld2000-2d yield function is employed to describe the experimentally measured in-plane plastic anisotropy of dual-phase steel. Additionally, the YLD2004-18p yield function is fully calibrated by full-field CP-based virtual tests of dual-phase steel. These models are implemented into the ABAQUS/UMAT subroutine to perform forming simulations. Hence, a comparative study of physical tests and virtual tests based sheet forming simulation of multi-phase materials is conducted.

2.4. Kinematic hardening model

For the constitutive modelling of hardening behaviour, isotropic hardening models are conventionally adopted to simply expand the size of the yield surface with the increasing plastic strain. However, materials generally experience a reverse tension–compression loading path during the deep drawing process. For instance, sheet metals pass through a die radius. During these loading paths, complex kinematic hardening behaviours like the Bauschinger effect, transient hardening, and permanent softening are observed. Springback is very sensitive to these hardening behaviours. Therefore, to obtain accurate springback analysis, these behaviours need to be described by the kinematic hardening model. Here, a two-surface model proposed by Ghaei and Taherizadeh (2015) is utilized to describe the kinematic hardening of dual-phase steels by controlling the movement of the yield surface within the bounding surface. This model is modified from the classical YU model proposed by Yoshida and Uemori (2002, 2003) and Yoshida et al. (2015) and shows better accuracy in predicting significant transient hardening behaviour, which is commonly observed in dual-phase steel (Marcadet and Mohr, 2015; Eghtesad and Knezevic, 2020; Hérault et al., 2021). This model consists of a yield surface denoted as f_y and a bounding surface. The yield surface is given by:

$$f_y(\sigma - \alpha) - y = 0 \tag{14}$$

where σ is the Cauchy stress tensor in the current configuration, and α is the backstress tensor that determines kinematic hardening. y is the initial yield stress of the material. To describe the evolution of the backstress tensor during plastic deformation, the rate of the backstress tensor is decomposed as $\dot{\alpha} = \dot{\alpha}_1 + \dot{\alpha}_2$. $\dot{\alpha}_1$ determines the relative movement between the yield surface and bounding surface, and $\dot{\alpha}_2$ determines the movement of the bounding surface. The $\dot{\alpha}_1$ is a function of the rate of equivalent plastic strain $\dot{p}$ and given by,

$$\dot{\alpha}_1 = \gamma_1 \left(\frac{b_0 + r - y}{y}(\sigma - \alpha) - \alpha_1 \right) \dot{p} \tag{15}$$

where γ_1 is a material constant that needs to be calibrated. $\boldsymbol{\alpha}_1$ is the offset tensor from the central point of the yield surface to the bounding surface. The $\dot{\boldsymbol{\alpha}}_2$ also is a function of the $\dot{p}$ and is given by:

$$\dot{\boldsymbol{\alpha}}_2 = \gamma_2 \left(\frac{c_2}{y}(\boldsymbol{\sigma} - \boldsymbol{\alpha}) - \boldsymbol{\alpha}_2 \right) \dot{p} \tag{16}$$

where c_2 and γ_2 are calibrated material constants. $\boldsymbol{\alpha}_2$ is the offset tensor from the original point to the central position of the bounding surface. The bounding surface is denoted as F and is given by,

$$F\left(\Sigma - \boldsymbol{\alpha}_2 \right) - b_0 - r(p) = 0 \tag{17}$$

where Σ is the stress tensor on the bounding surface in the current configuration, and $\boldsymbol{\alpha}_2$ is the backstress tensor for the movement of the bounding surface. b_0 is a material constant that defines the initial size of the bounding surface. The expansion of the bounding surface with the increasing equivalent plastic strain p is determined by the variable r, which is a function of p and is given by,

$$r(p) = Q\left[1 - \exp\left(-bp\right)\right] \tag{18}$$

where the Q and b are parameters used to fit the tension–compression stress–strain curves in cyclic loading.

3. Materials, mechanical tests and forming experiments

This section characterizes the microstructure of the case DP steels DP780 and DP980. The microstructural information is used to establish the dual-phase RVEs, enabling the development of the full-field crystal plasticity modelling laboratory for virtual tests under various loading scenarios. Additionally, Uniaxial and biaxial tensile tests are designed and conducted to obtain the anisotropic plastic responses in various stress states, and the reverse tension–compression tests are designed and conducted to investigate the kinematic hardening behaviour of the DP steels. The mechanical test results are further used to verify the accuracy of the virtually tested results and calibrate the advanced phenomenological constitutive models. Finally, U-bending forming experiments and simulations are introduced to verify the accuracies of advanced constitutive models calibrated by the virtual and physical tests.

3.1. Microstructure characterization

The as-received materials are DP780 and DP980 sheets with thicknesses of 2 mm and 1 mm, respectively. The two types of cold-rolled dual-phase steels with different fractions of soft ferrite phase and hard martensite phase are provided by Baosteel. To obtain the texture data, crystalline morphology, and phase distribution, electron-backscattered diffraction (EBSD) characterization is conducted on the RD-TD (rolling direction - transverse direction) plane of the DP780 and DP980 specimens. The specimens are cut from the center zone on the as-rolled sheet to better represent the overall microstructure property of the sheets. The employed SEM-EBSD system is a ZEISS® GeminiSEM 460 field emission SEM equipped with an Oxford Symmetry S2 EBSD detector. The scanning area is 200 μm × 200 μm and the scanning step is 0.25 μm, and hence, collected 640,000 data index points in total. The open-source EBSD data post-processing software MTEX is used to generate EBSD inverse pole figures (IPF), band contrast (BC) maps, and pole figures (PF). The microstructure characterization of DP780 is presented in Fig. 2. Fig. 2a shows the EBSD map plotted with RD IPF colour of DP780 sheet. The crystal structure of the martensite phase is a body-center cubic or body-centered tetragonal structure, which generally shows almost the same diffraction pattern as the body-center cubic ferrite phase during the EBSD scanning. Therefore it is difficult to separate the ferrite and martensite phases using the EBSD diffraction pattern. Here, the BC map illustrated in Fig. 2b is utilized to identify the phase distribution, in which the region with high BC value is soft ferrite phase and with low BC value is hard martensite phases (Li et al., 2019; Choi et al., 2013). The threshold of the BC value is determined by the overlapping region of two Gaussian functions for the two peaks of the BC value frequency distribution curve as illustrated in Fig. 2c. The ferrite and martensite phase distribution map of DP780 using the threshold value of 134 is indicated in Fig. 2d, where the fractions of the ferrite and martensite phases are 79.48% and 20.52%, respectively. The corresponding separated EBSD IPF maps of single ferrite and martensite phase are shown in Fig. 2e and f, respectively. A similar texture is observed in [111] pole figures of the separated ferrite and martensite phases, as illustrated in Fig. 2g. Fig. 2h shows the orientation density function (ODF) plotted ϕ_1- Φ orientation density maps as sections through the reduced Euler space for cubic-orthorhombic symmetry (constant ϕ_2 sections, 0° to 90° in 5° steps, Euler angles in Bunge's convention). A typical cold rolling texture of BCC structure with α fibre and γ fibre is observed and the highest texture intensity is located at the γ fibre component {111}⟨112⟩.

The microstructure characterization of DP980 is illustrated in Fig. 3. The EBSD map with RD IPF colour is shown in Fig. 3a. As illustrated in Fig. 3c, the BC threshold value of 138 is determined by the Gaussian fitting of the BC maps shown in Fig. 3b. The corresponding phase distribution map is indicated in Fig. 3d, where the fractions of the ferrite and martensite phases are 53.86% and 46.14%, respectively. Clearly, as compared to DP780, the ferrite phase fraction is much lower, while the martensite phase fraction is much higher. The separated EBSD IPF map of the ferrite and martensite phases is shown in Fig. 3e and f, respectively. A similar texture is observed in their [111] pole figures as shown in Fig. 3g. Also, the similar cold rolling texture with α and γ fibre as DP780 is observed in the orientation density map of DP980 as plotted in Fig. 3h. However, the texture intensity of DP980 is lower than DP780, and the highest texture intensity is located at the component {111}⟨110⟩ of both the α and γ fibres.
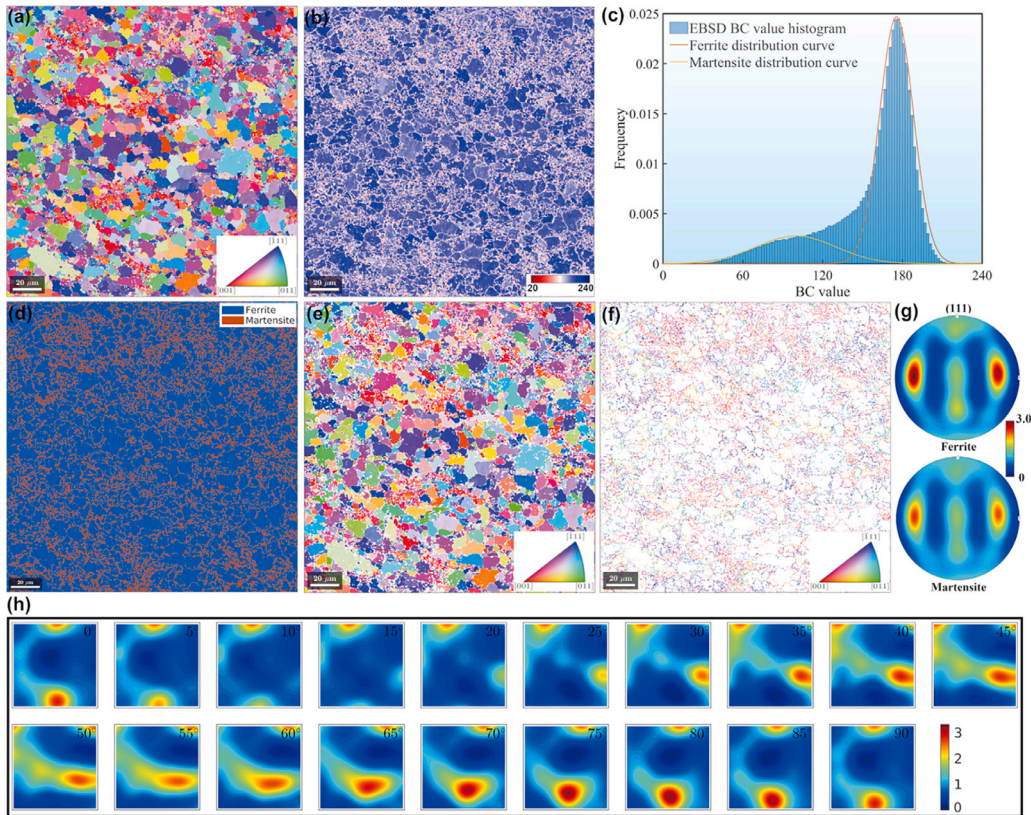
Fig. 2. Microstructure characterization of DP780: (a) EBSD map with IPF colour; (b) BC value map; (c) the spatial distribution of BC values and Gaussian fit for ferrite and martensite phase; (d) the phase distribution map; the filtered EBSD map based on the BC values for (e) ferrite phase (f) martensite phase; (g) the pole figures for ferrite and martensite phase; (h) ODF based orientation density maps as sections through the reduced Euler space for cubic-orthorhombic symmetry.

3.2. Representative volume element

To obtain accurate simulations in the full-field multi-phase crystal plasticity modelling, the features of the realistic microstructure, such as crystalline morphology, texture and phase distribution should be accessible in the synthetic RVE. The crystalline morphology is characterized by the grain shape distribution using EBSD data as illustrated in Figs. 4a and 5a for DP780 and DP980, which plot the statistical frequency of the grain shape aspect ratio of the length of each grain in TD divided by in RD denoted as TD:RD. It is seen that the majority of the shape aspect ratios are in the range from 0.6 to 0.8, i.e., the grain shape is slightly elongated along RD due to the in-plane strain compression deformation in the cold rolling process. According to the study of the previous work (Liu et al., 2020c), the grain aspect ratio of DP steels in the range from 1:1:1 to 1:0.5:0.5 used in the CP simulations has negligible influences on both the yielding point and strain hardening behaviour. Here, using the open-source polycrystal RVE generation software neper (Quey et al., 2011), grain shape aspect ratios of RD:TD:ND = 1:0.65:0.65 and RD:TD:ND = 1:0.7:0.7 are employed in the generation of RVE with 3000 grains of DP780 and DP980. 3000 grain orientations are calculated by ODF, and plotted using IPF colour in the RVEs, as illustrated in Figs. 4b and 5b. The mesh resolution of the RVE utilized in the CP simulations is $125 \times 125 \times 125$ Fourier points (total of 1,953,125 voxels). The phase fraction of ferrite and martensite in the RVEs are defined as identical to the EBSD characterization, namely, the phase distribution of DP780 RVE with 80.02% ferrite phase and 19.98% martensite phase, and DP980 RVE with 54.24% ferrite phase and 45.76% martensite phase, as illustrated in Figs. 4c and 5c, respectively. The [111] pole figures of the separated ferrite and martensite phase in RVEs are indicated in Figs. 4d and 5d for DP780 and DP980, which indicate that the synthetic texture is almost same as the experimental EBSD characterization.

3.3. Mechanical tests: uniaxial tension, biaxial tension, and reverse tension–compression

Both uniaxial and biaxial tensile tests are performed to characterize the plastic anisotropy of DP780 and DP980. Fig. 6a shows the experimental set-up, where the tests are conducted in the electromechanical Herculi® NOIA-150 biaxial testing machine with a maximum loading capability of 150 kN. A stereo DIC system is employed to measure the strain field of the gauge area of the specimen. To ensure synchronous data acquisition in loading data and strain field measurement, the two cameras are triggered by
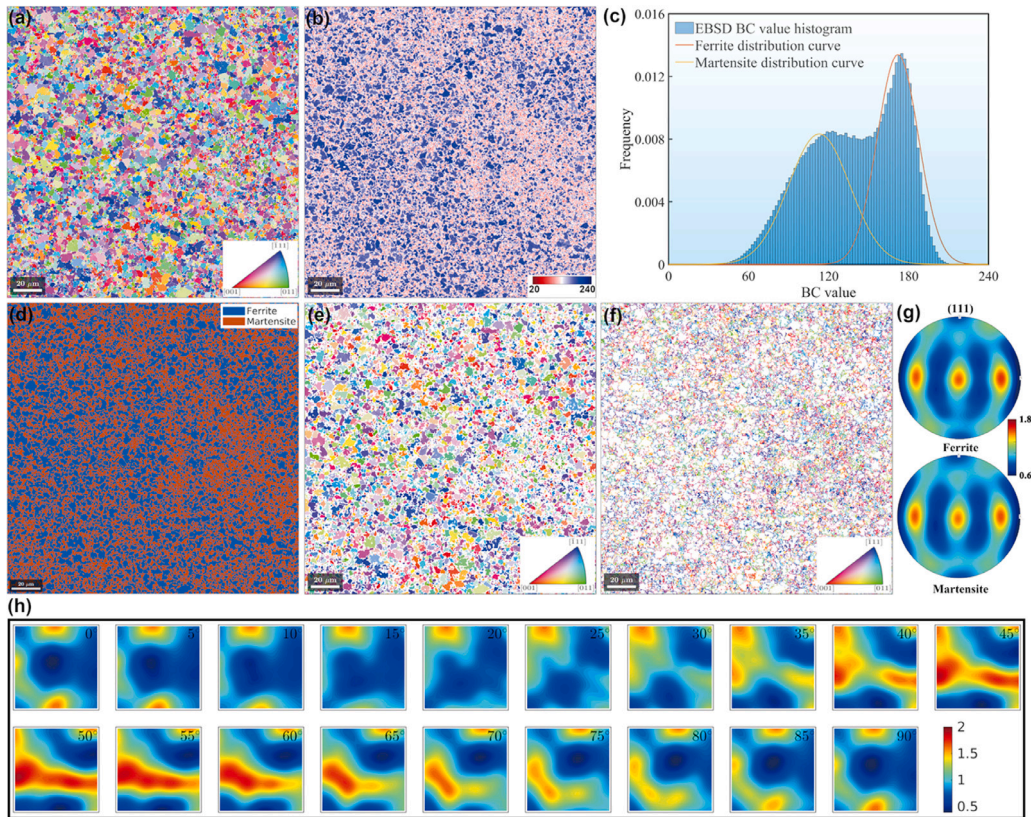
Fig. 3. Microstructure characterization of DP980: (a) EBSD map with IPF colour; (b) BC value map; (c) the spatial distribution of BC values and Gaussian fit for ferrite and martensite phase; (d) the phase distribution map; the filtered EBSD map based on the BC values for (e) ferrite phase (f) martensite phase; (g) the pole figures for ferrite and martensite phase; (h) ODF based orientation density maps as sections through the reduced Euler space for cubic-orthorhombic symmetry.
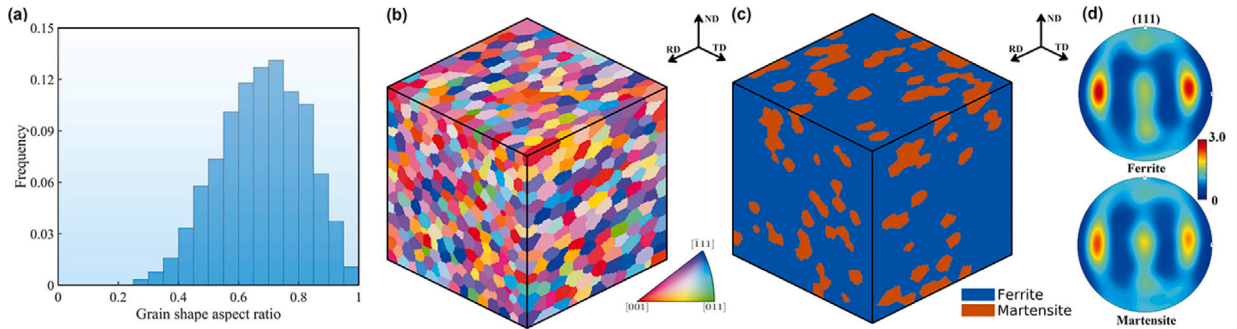
Fig. 4. RVE building for DP780: (a) Statistical frequency of the grain shape aspect ratio of the length of each grain in TD divided by in RD for DP780; (b) IPF map in DP780 RVE; (c) the phase distribution in DP780 RVE; (d) the [111] pole figures for ferrite and martensite phase in DP780 RVE. (For interpretation of the references to colour in this figure legend, the reader is referred to the web version of this article.)

the same signal of the loading data acquisition output by the biaxial testing machine. The time interval of the data acquisition is 0.1 s.

Biaxial tensile tests with cruciform specimens were performed to measure the biaxial yield stress of the DP steels. The geometrical dimension of the cruciform specimen was designed by following the ISO:16842:2014 standard, as given in Fig. 6b (Kuwabara and Sugawara, 2013; Hanabusa et al., 2013; Deng et al., 2015). The loading rate was controlled with a constant von Mises equivalent plastic strain rate at 2×10^4/s for all stress paths. Here, the cruciform specimens were subjected to proportional loading with the force ratios of RD:TD = 2:1, 4:3, 1:1, 3:4, and 1:2. The procedure for determining a contour of plastic work is as follows. The uniaxial tensile true stress versus true plastic strain curve ($\sigma_0 - \epsilon_0^p$ curve) measured for the RD of the test sample was selected as the reference
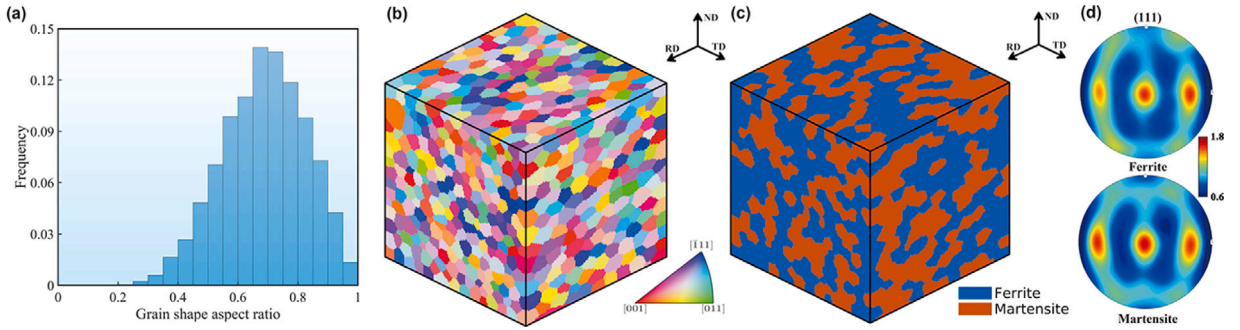
Fig. 5. RVE building for DP980: (a) Statistical frequency of the grain shape aspect ratio of the length of each grain in TD divided by in RD for DP980; (b) IPF map in DP980 RVE; (c) the phase distribution in DP980 RVE; (d) the [111] pole figures for ferrite and martensite phase in DP980 RVE.
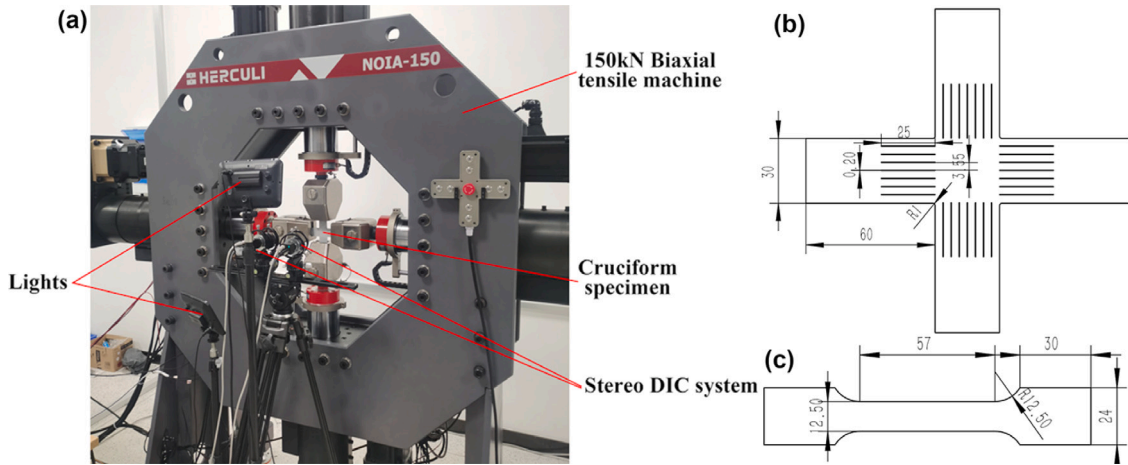

Fig. 6. Biaxial tensile tests: (a) The schematics of the electromechanical Herculi® NOIA-150 biaxial testing machine and stereo DIC system used for the uniaxial and biaxial tensile tests. (b) The dimension of cruciform specimen used in biaxial tensile tests following ISO:16842:2014 standard; (c) The dimension of specimen used in uniaxial tensile tests following ASTM-E8 standard.

datum for work hardening, and the plastic work per unit volume, W_0^p, consumed until the tensile strain reached particular values of ϵ_0^p was determined. The respective stress points on each linear stress path, at which the same plastic work as W_0^p was consumed, form a contour of plastic work associated with ϵ_0^p.

The uniaxial tensile tests were performed using the ASTM-E8 standard (dimension shown in Fig. 6c in the directions of 0°, 15°, 30°, 45°, 60°, 75°, and 90° inclined from the RD of the test sample. The strain rate was approximately 1×10^{-4}/s (crosshead speed: 0.005 mm/s). In addition, the uniaxial loading-unloading-loading (ULUL) cycle tensile test is conducted on the specimen aligned with RD to characterize the degradation of elastic modulus under various strain levels.

The tension–compression tests are conducted on a SINOTEST 100 kN universal testing machine at a cross-head velocity of about 1 mm/min. Fig. 7a shows the experimental setup, where a fixture is applied to avoid buckling during the compression process. Two 1 mm lubricant Teflon sheets are attached to the specimen surface to reduce the friction force. A stereo DIC system is used to measure the strain field through the observation window of the fixture during the tension and compression as illustrated in Fig. 7b and c. The geometry of the specimens is shown in Fig. 7d.

3.4. U-bending experiments and simulations

DP780 sheets with a thickness of 2 mm and DP980 sheets with a thickness of 1 mm were cut into a 300 mm × 30 mm blank, and the long side is aligned with RD, which is utilized to perform the U-bending tests. Fig. 8a and b show the schematics and dimensions of the tools. The U-bending tests tool consists of a punch, a die and lower and upper plates separated by a blank holder using two groups of springs. The blank holder plate is designed to have vertical movement along the two guide posts and four spring guides that are attached to the lower plate. The lower springs are utilized to support the blank holder at a small distance from the die surface, ensuring convenient insertion of the blank. The upper springs are utilized to transmit the blank holder force exerted on the blank holder plate. The lower plate was used to fix the U-bending tool on a 500 kN hydraulic press machine. During the draw-bending process, the upper plate is firstly pressed by the hydraulic press machine until the 6500 N blank holder force is
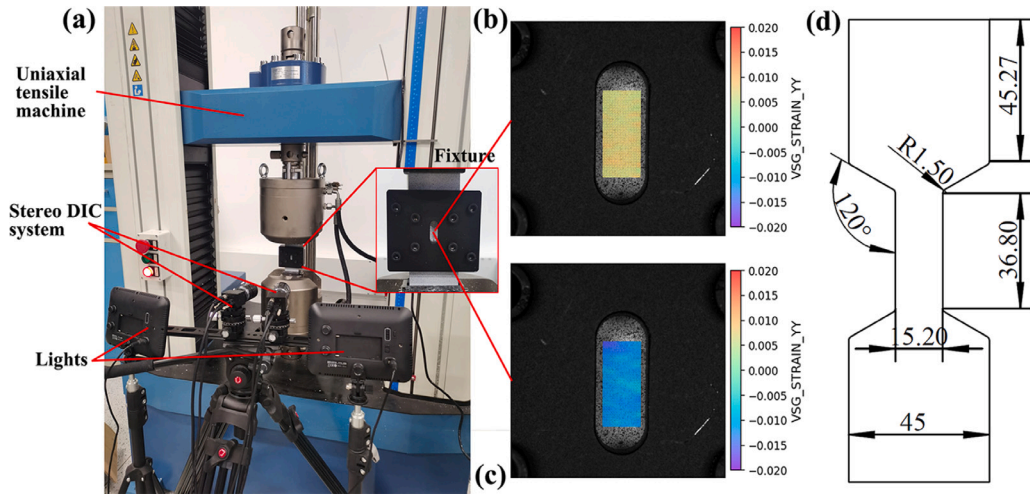
Fig. 7. Tension–compression tests: (a) The schematics of the experimental setup for reverse tension–compression tests consisting of a uniaxial tensile machine, a stereo DIC system and an anti-buckling fixture. The strain field was measured by DIC through the observation window of the fixture during (b) tension and (c) compression. (d) The dimension of the specimen used in the TC tests.
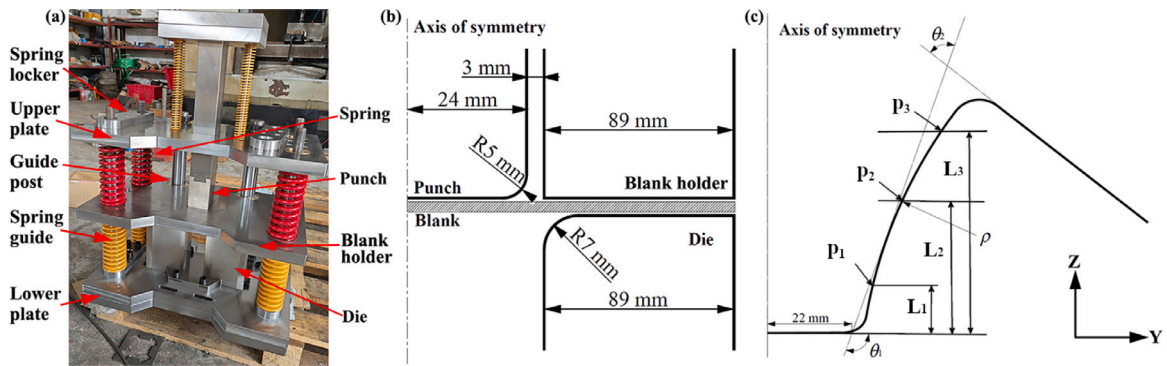

Fig. 8. U-bending experiments: (a) The schematics of tooling system for U-bending tests. (b) The dimensions of the punch, blank holder and die in the tooling system. (c) The measurement method for the angle θ_1, θ_2 and curvature radius ρ from the profile of a U-shaped specimen after springback.

reached, and then the position of the upper plate is fixed by the spring locker to constant the force. Subsequently, the punch is pressed down using a speed of 1 mm/s until its stroke reaches 71.8 mm. Finally, the punch and upper plate are moved up to allow the springback of the formed part. The profile, angle θ_1, θ_2 and curvature radius ρ of the U-shaped part after springback shown in Fig. 8c are measured to assess the accuracy of the simulations. The curvature radius ρ is calculated using the three points (p_1, p_2 and p_3), and their positions are determined by the length of L_1, L_2 and L_3. The $L_1 = 10$ mm, $L_2 = 35$ mm and $L_3 = 60$ mm is used in DP780 springback specimens and the $L_1 = 10$ mm, $L_2 = 27.5$ mm and $L_3 = 45$ mm is used in DP980 springback specimens. For exact comparison, the calculation procedure in experiments and simulations are the same.

The U-bending and springback simulations were conducted in ABAQUS 2020/implicit using two constitutive models, i.e. virtual tests calibrated Yld2004-18p and experimental test calibrated Yld2000-2d associated with the two-surface kinematic hardening model described in Section 2.4. These models are successfully implemented into the ABAQUS/UMAT user subroutine. Half of the blank and tools are modelled using the symmetry boundary condition. The tools are modelled as the analytical rigid body. For the Yld2004-18p model, the eight-node solid elements with reduced integration (C3D8R) were employed for the blank with length, width and height equal to 0.5, 0.5 and 0.25 mm. For the Yld2000-2d model, the four-node shell elements with reduced integration (S4R) were employed for the blank with length, width equal to 0.5 and 0.5 mm, and nine integration points for the thickness direction were employed. The Coulomb friction law with a friction coefficient of 0.1 was employed to describe the contact behaviour between the tools and a blank. The forming simulation of the U-bending includes three steps: (1) apply blank holder force (2) draw bending (3) springback by removing all contact.
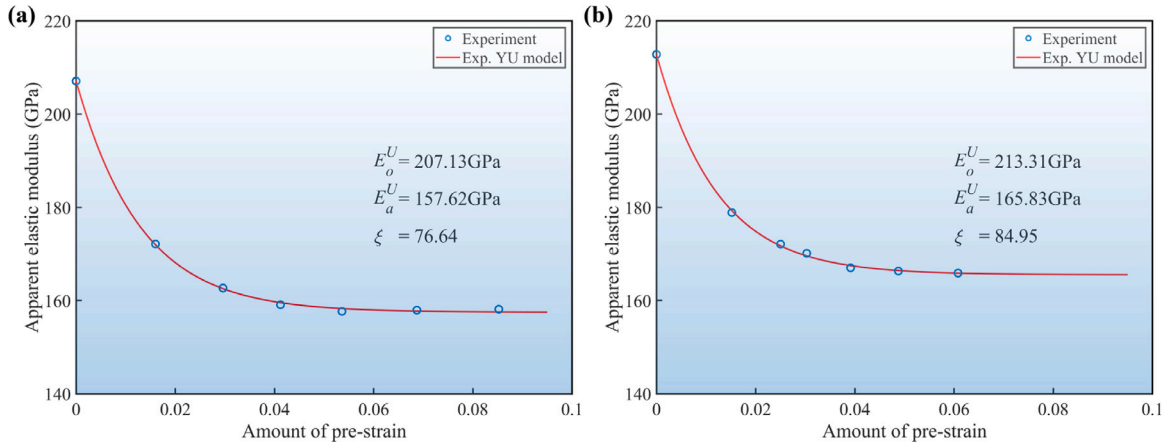
Fig. 9. The experimental degradation of elastic modulus in the unloading process with various pre-strain uniaxial tension for (a) DP780 and (b) DP980. The results of experiments are used to calibrate the corresponding YU model.

4. The experimental mechanical tests

In this section, the experimental results with respect to non-linear elastic modulus, plastic anisotropy and kinematic hardening of DP steels are introduced and discussed. These data are utilized to verify the accuracy of the virtual tests and to calibrate the experiments based advanced constitutive model.

4.1. The experimental kinematic hardening and non-linear elastic behaviour

The evolution of the elastic modulus of the DP steels with various prestrain levels is characterized by the uniaxial loading-unloading-reloading (ULUL) tests. The initial elastic modulus is calculated by the slop from an initial point to 50 MPa, and the actual elastic modulus in the unloading process with various pre-strain is calculated by the slop of a straight line drawn between the two stress–strain points at the initial unloading and completely unloading state. Fig. 9a and b show the degradation of elastic modulus obtained by the experimental ULUL tests for DP780 and DP980, respectively. It is seen that the elastic modulus of DP780 is reduced from the initial value of 207.1 GPa to a saturated value of 158.1 GPa with the increasing of tensile pre-strain. For the DP980, the elastic modules are reduced from 213.3 GPa to 165.7 GPa. The experimental material sampling points are used to calibrate the corresponding YU models and the parameters are also plotted in Fig. 9a and b. A good agreement between the experimental results and YU models is achieved with respect to the evolution of the elastic modulus.

Fig. 10a and b show the true stress–strain curves in the reverse uniaxial tension–compression–tension tests with maximum tension and compression strain of 2.5% and −2.5% along RD of DP780 and DP980, respectively. Fig. 10c and d show the results of uniaxial reverse uniaxial tension–compression tests along RD with tensile pre-strain of 2.5%, 5% and 7.5% of DP780 and DP980, respectively. The significant transient Bauschinger effect is observed in the DP steels, i.e. the re-yielding strength is significantly reduced when the loading direction is reversed.

4.2. The experimental plastic anisotropy

Following the ASTM-E8 standard, the experimental true stress–strain curves in the uniaxial tensile tests aligned with 0°, 15°, 30°, 45°, 60°, 75°, and 90° from RD for the DP780 and DP980 are obtained and illustrated in Figs. 11a and 12a, respectively. All the stress–strain curves show the typical strain hardening behaviour of DP steels such as no obvious yield points, continuous yielding and very high strain hardening. The highest and lowest strengths are observed in TD and 15° for DP780, and they are in 75° and RD for DP980. At the stage close to fracture during the uniaxial tension, the DIC measured strain field for ε_{yy} aligned with the loading direction in the specimens from RD to TD are illustrated in Figs. 11b and 12b for DP780 and DP980, respectively. The shear bands with an angle of about 45° to the loading directions are observed in all the specimens.

The evolution of the r-value, the ratio of the plastic strain rate aligned with width to thickness direction, during the uniaxial tension is obtained by the DIC system. Here, the strain increment of $\Delta\varepsilon_{xx}$ and $\Delta\varepsilon_{yy}$ measured by the DIC system between the each frames are used to approximately calculate the r-value by $r = -\frac{\Delta\varepsilon_{xx}}{\Delta\varepsilon_{xx}+\Delta\varepsilon_{yy}}$, instead of calculating the r-value using the strain rate with $r = -\frac{\dot{\varepsilon}_{xx}}{\dot{\varepsilon}_{xx}+\dot{\varepsilon}_{yy}}$. Figs. 11d and 12d show the r-value field of the DP780 and DP980 for the specimens from RD to TD at the stage of the plastic strains of 0.1 and 0.05 measured by the DIC system. The evolution of the r-value in the DP780 and DP980 specimens at various plastic strain levels are plotted in Figs. 11c and 12c. The typical variation of the r-values for the α and γ textures are observed in DP780 in which the r-value is highest at an angle of 45° and relatively lower in RD and TD. For the DP980 specimens, the highest and lowest r-values are at 60° and 0°, respectively. In addition, the r-values of the DP780 specimens in all directions are
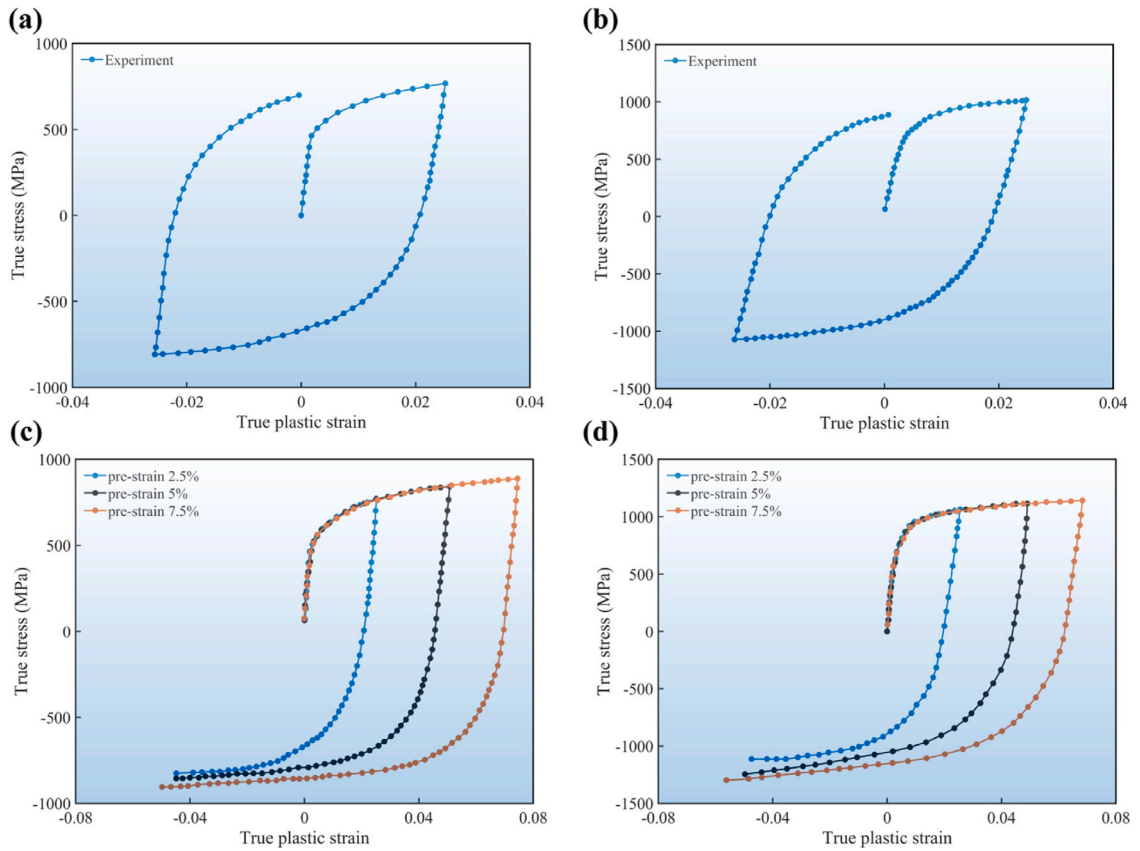
Fig. 10. The true stress versus true strain curves in the 1.5 cycles of uniaxial tension and reverse compression loading obtained by the experiment for (a) DP780 and (b) DP980; The true stress versus true strain response in three groups of uniaxial tension and reverse compression loading with various prestrain levels obtained by the experiments for (c) DP780 and (d) DP980.

gradually decreased with the increasing of plastic strain, while they are kept approximately steady in DP980. This may be attributed to the high volume fraction of the hard martensite phase in DP980 restricts the slip of the soft ferrite phase and results in a small texture evolution.

Following the ISO:16842:2014 standard, the strain ε_{xx} and ε_{yy} fields with various stress ratios at equivalent plastic strain of 0.015 and 0.007 for DP780 and DP980 are measured by the DIC systems and shown in Fig. 13a and b. It can be seen that the strain field is approximately uniform on the central gauge area of the cruciform, and hence the stress distribution of the gauge area is also uniform. Accordingly, the evolution of the yield locus of DP780 and DP980 in biaxial stress state with various stress ratios are measured by the cruciform specimens at various equivalent plastic strain and illustrated in Fig. 13a and b. It is seen that the strain hardening level in the equibiaxial stress state is higher than that in the uniaxial stress state.

5. The results of virtual tests

In this section, the results of virtual tests with respect to the non-linear elastic modulus, plastic anisotropy and kinematic hardening of DP steels are introduced and verified by the corresponding experimental results. These data are utilized to calibrate the virtual tests based advanced constitutive model.

5.1. Material constants in crystal plasticity modelling

To obtain the accurate crystal plasticity parameters, an iterative optimization procedure is conducted in the virtual reverse uniaxial tension–compression–tension tests with maximum tension and compression strain of 2.5% and −2.5% along RD of DP780 and DP980 utilizing the RVE to minimize the deviation of the predicted stress–strain curves from the experimental ones, as illustrated in Fig. 15a and b. Since the volume fractions of ferrite and martensite phases are different in DP780 and DP980, the parameters of CP model in ferrite and martensite phases could be obtained in the iterative optimization procedure until the deviations between the predicted stress–strain curves and experimental ones in DP780 and DP980 are both minimized. The single crystal elastic stiffness coefficients for the ferrite phase are obtained by atomic force microscopy (AFM) measurements which are taken from Ref. Tasan
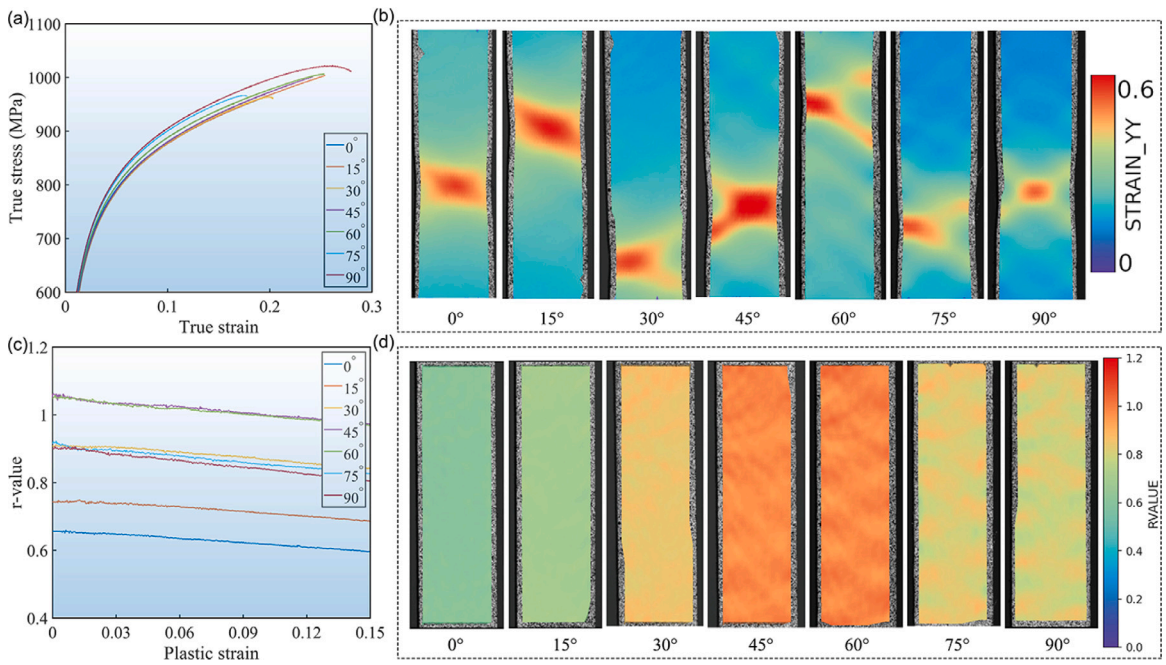
Fig. 11. (a) The true stress–strain curves of the DP780 in uniaxial tension from RD to TD at an interval of 15°, (b) the DIC measured contour maps of the true strain aligned loading direction for the DP780 specimens close to fracture in uniaxial tension from RD to TD at an interval of 15°, (c) the evolution of the r-value for the DP780 specimens in the uniaxial tension from RD to TD at an interval of 15°, (d) the DIC measured contour maps of the r-value at plastic strain of 0.1 for the DP780 specimens in the uniaxial tension from RD to TD at an interval of 15°.
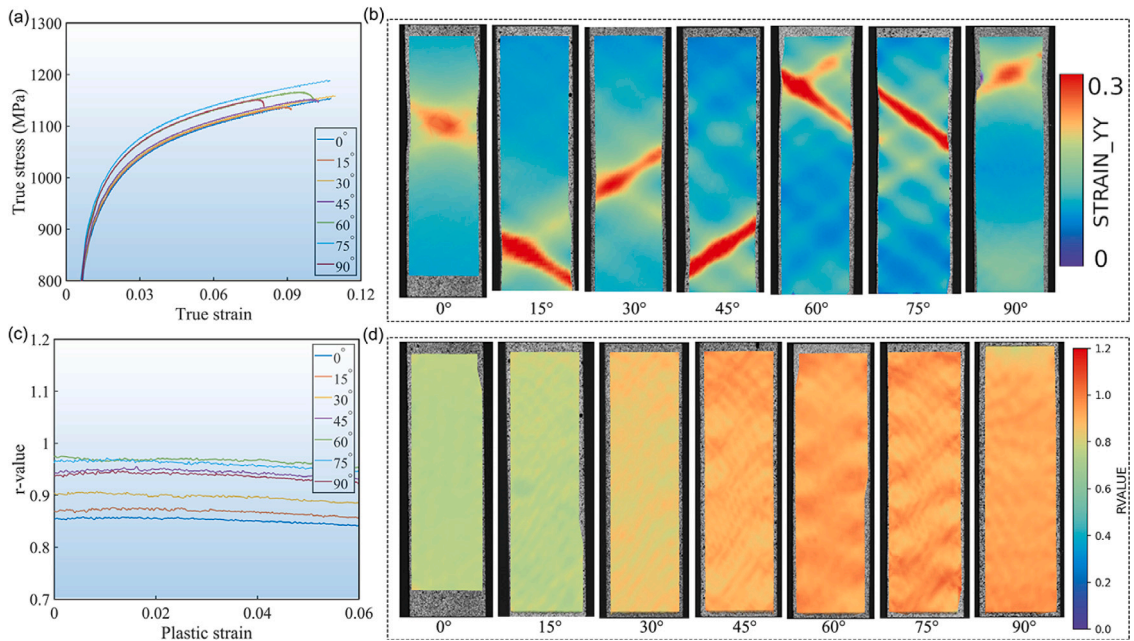

Fig. 12. (a) The true stress–strain curves of the DP980 in uniaxial tension from RD to TD at an interval of 15°, (b) the DIC measured contour maps of the true strain aligned loading direction for the DP980 specimens close to fracture in uniaxial tension from RD to TD at an interval of 15°, (c) the evolution of the r-value for the DP980 specimens in the uniaxial tension from RD to TD at an interval of 15°, (d) the DIC measured contour maps of the r-value at plastic strain of 0.05 for the DP980 specimens in the uniaxial tension from RD to TD at an interval of 15°.

et al. (2014). The crystal elastic constants for martensite phases are determined by fitting the CP predicted curves to the experimental stress–strain response of DP780 and DP980 in elastic deformation as illustrated in Fig. 14a. The experimental initial elastic modulus
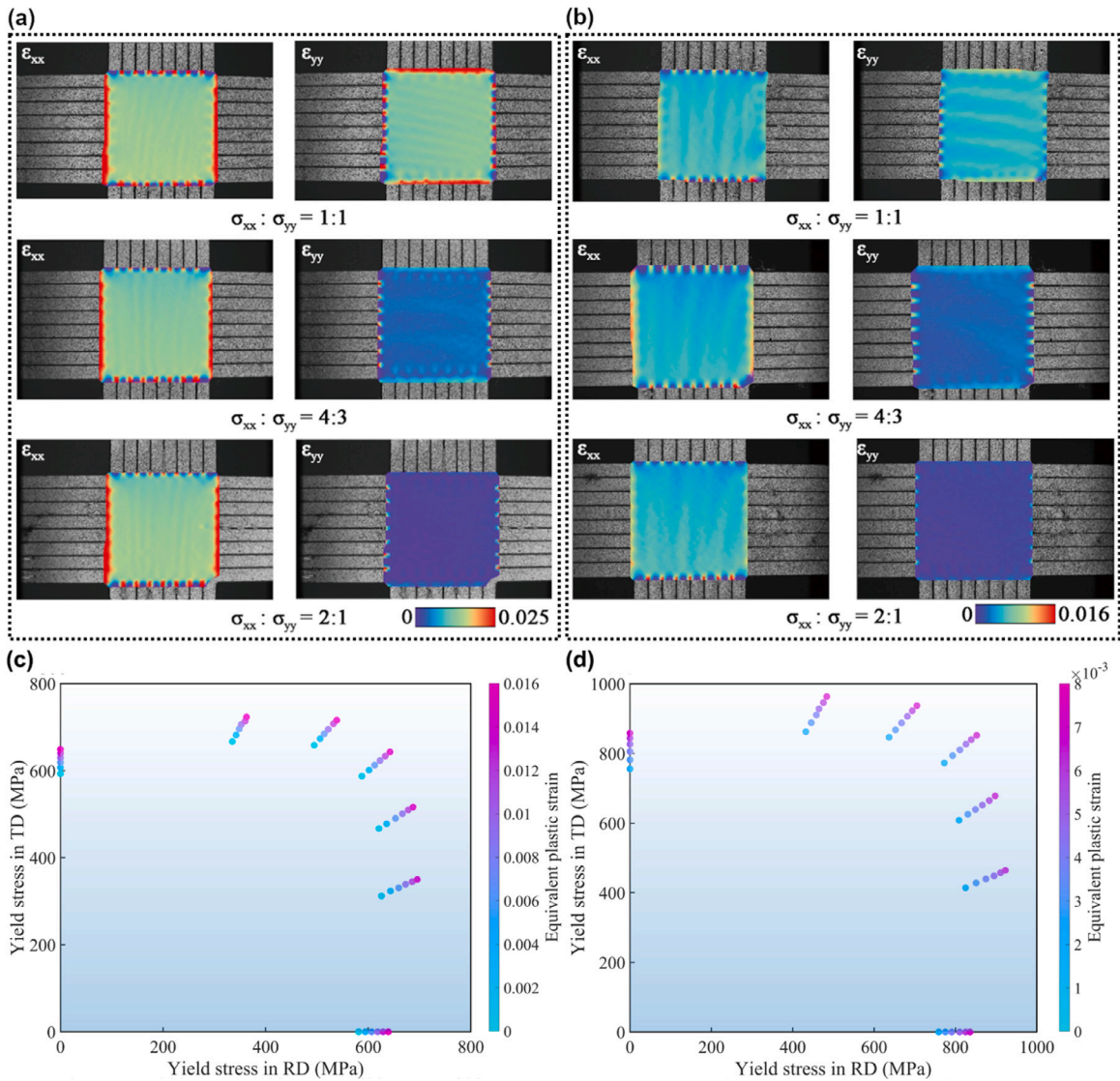
Fig. 13. the DIC measured contour maps of the true strain aligned RD and TD in the biaxial tensile tests utilizing the stress ratio of $\sigma_{xx} : \sigma_{yy}$ = 1:1, 4:3 and 2:1 for the (a) DP780 and (b) DP980 specimens, and the biaxial yield stress points at various equivalent plastic strains in RD-TD planes for the (c) DP780 and (d) DP980 specimens.

of DP980 is 213.31 GPa with 46.14% martensite phase, which is higher than 207.13 GPa DP780 with 20.52% martensite phase. The Fig. 14b shows the 1.5 cycles of uniaxial tension–compression–tension loading obtained by virtual test using the optimized parameters for DP780, DP980, single ferrite and martensite phase. The transient Bauschinger effect and reduction of yield stress at re-yielding point are successfully predicted by the CP model thanks to the backstress terms on slip systems explicitly included in the hardening model. The obtained optimal parameters for the ferrite and martensite phase are documented in Table 1. To further verify the accuracy of the CP model, the stress–strain curves in reverse tension–compression with various maximum tension strains of DP780 and DP980 are predicted and in comparison with the experimental results, as illustrated in Fig. 15c and d. It is seen that the crystal plasticity modelling using one group of parameters could accurately predict the kinematic hardening behaviour of the DP steels with various volume fractions of ferrite and martensite phases under various reverse tension–compression loading conditions, i.e. this model could be generally applied in various dual phase steels.

Additionally, the evolution of the elastic modulus in the unloading process under the uniaxial tension with various prestrain levels is predicted by the virtual tests. The stress–strain curves during the ULUL process predicted by the virtual tests are in good agreement with experiments as illustrated in Fig. 16. Fig. 17 shows the comparison of the degradation of elastic modulus obtained by the experimental ULUL tests and virtual tests. A good agreement is achieved with respect to the evolution of the elastic modulus. The degradation of elastic modules could be described by the CP simulations because the backstress items are involved in the unloading
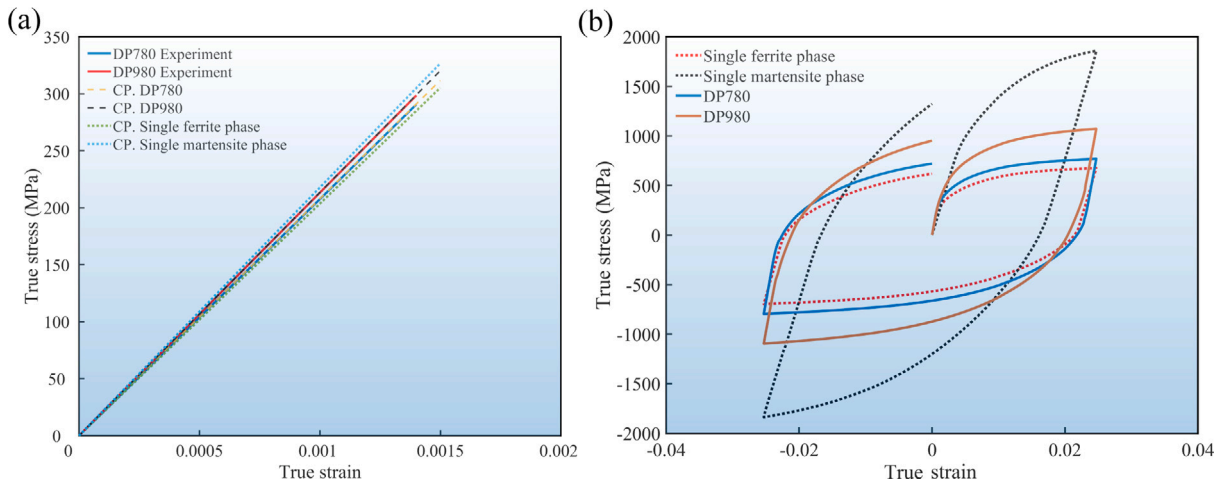
Fig. 14. (a) The elastic response obtained by virtual test for DP780, DP980, single ferrite and martensite phase and compared with the experimental results. (b) The comparison of the true stress versus true strain curves in the 1.5 cycles of uniaxial tension and reverse compression loading obtained by virtual test for DP780, DP980, single ferrite and martensite phase.
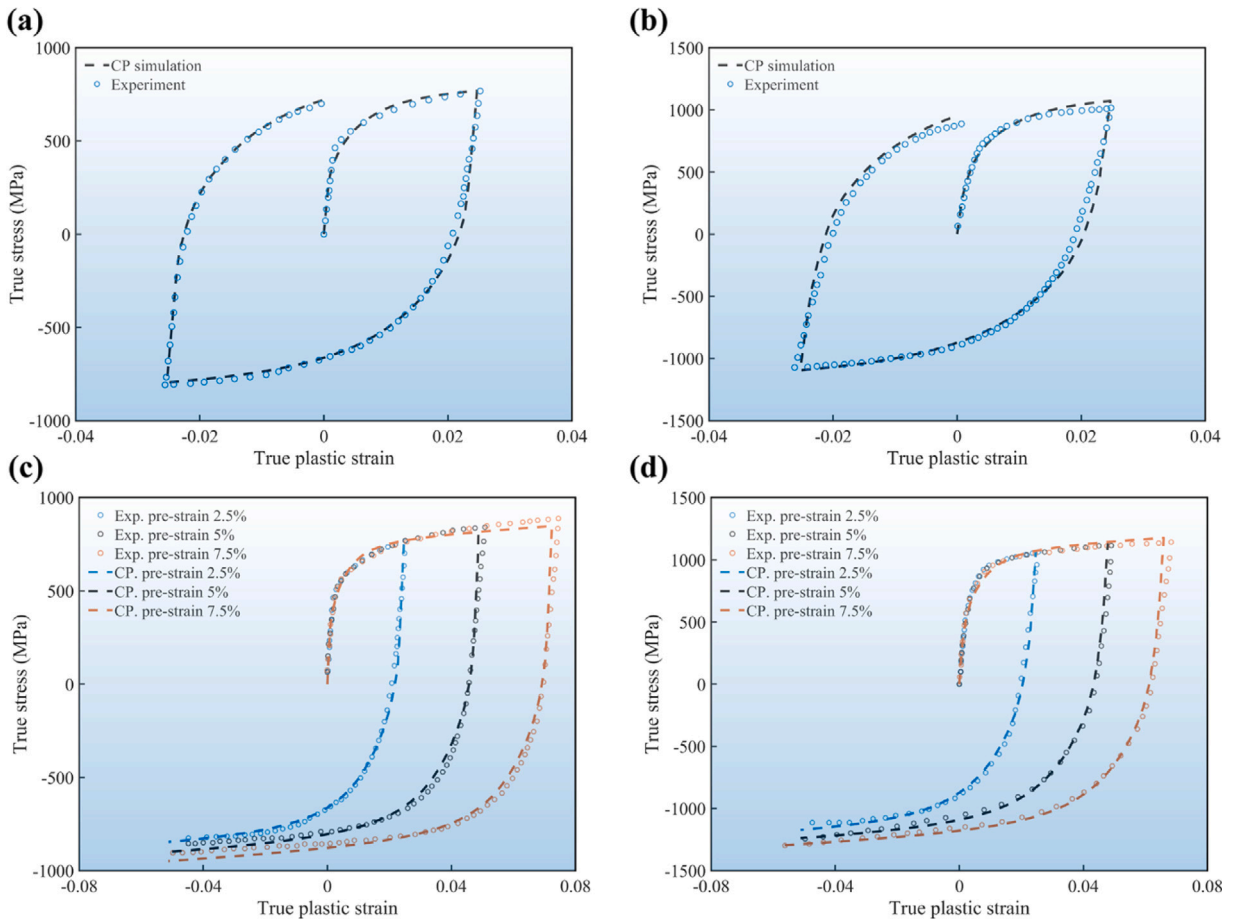

Fig. 15. The comparison of the true stress versus true strain curves in the 1.5 cycles of uniaxial tension and reverse compression loading obtained by virtual test and experiments for (a) DP780 and (b) DP980; The comparison of true stress versus true strain response in three groups of uniaxial tension and reverse compression loading with various prestrain levels obtained by virtual tests and the experiments for (c) DP780 and (d) DP980.
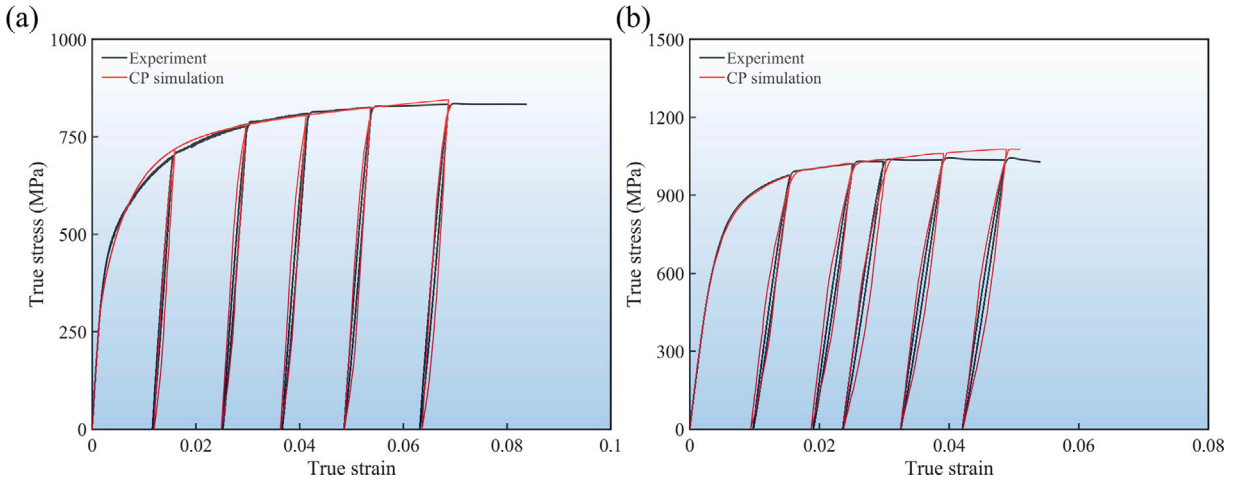
Fig. 16. The comparison of the experimental and virtual tests predicted strain–stress curves in ULUL process for (a) DP780 and (b) DP980.
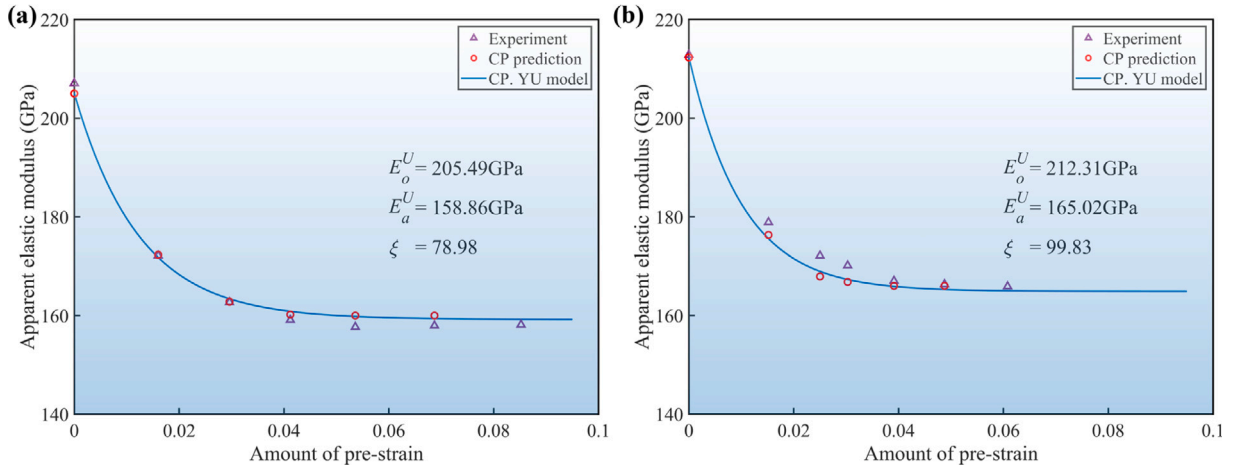

Fig. 17. The comparison of the experimental and virtual tests predicted degradation of elastic modulus in the unloading process with various pre-strain uniaxial tension for (a) DP780 and (b) DP980. The results of virtual tests are used to calibrate the corresponding CP-based YU model.

Table 1

The parameters of CP model for Ferrite and Martensite phase in DP steels.

Ferrite phase:						
C_{11} (GPa)	C_{12} (GPa)	C_{44} (GPa)	τ_0^s (MPa)	τ_1 (MPa)	θ_0 (MPa)	θ_1 (MPa)
233.3	135.5	118.0	108.2	30.1	79.9	54.1
τ_1^{bs} (MPa)	θ_0^{bs} (GPa)	θ_1^{bs} (MPa)	$\dot{\gamma}_0$ (s^{-1})			
50.4	30.2	5.98	0.0001			
Martensite phase:						
C_{11} (GPa)	C_{12} (GPa)	C_{44} (GPa)	τ_0^s (MPa)	τ_1 (MPa)	θ_0 (MPa)	θ_1 (MPa)
285.6	164.1	121.0	324.1	53.9	234.1	161.8
τ_1^{bs} (MPa)	θ_0^{bs} (GPa)	θ_1^{bs} (MPa)	$\dot{\gamma}_0$ (s^{-1})			
151.2	89.8	18.02	0.0001			

process, which is increased with the increase of the pre-strain during ULUL virtual tests. These data are further used to calibrate the parameters of the virtual tests based YU models, which are also plotted in Fig. 17.

5.2. The virtual tests for plastic anisotropy

In the virtual uniaxial tension loading in RD case, deformation is described in the $\bar{\bar{\mathbf{F}}}_{11}$ direction and the deformation in the $\bar{\bar{\mathbf{F}}}_{22}$ and $\bar{\bar{\mathbf{F}}}_{33}$ directions will be adjusted to a value such that the average PIOLA–KIRCHHOFF stress in that direction is zero. All other
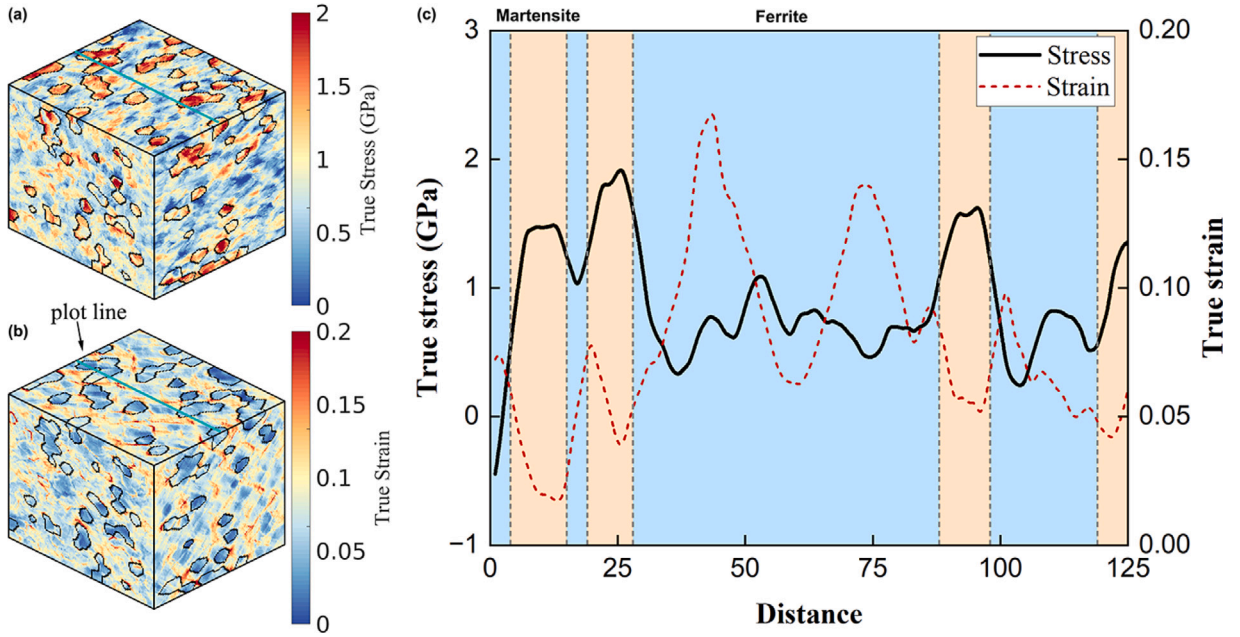
Fig. 18. (a) The distribution of true stress along the loading direction on the deformed RVE of DP780 at equivalent plastic strain of 0.1; (b) The distribution of true strain along the loading direction on the deformed RVE of DP780 at equivalent plastic strain of 0.1; (c) The variation of the true stress and strain in the mixed ferrite and martensite phase through the plot line.

components have no deformation (resulting potentially in stress):

$$\frac{\dot{\overline{\mathbf{F}}}}{10^{-3}\mathrm{s}^{-1}} = \begin{bmatrix} 1 & 0 & 0 \\ 0 & * & 0 \\ 0 & 0 & * \end{bmatrix} \quad \text{and} \quad \frac{\overline{\mathbf{P}}}{\mathrm{Pa}} = \begin{bmatrix} * & * & * \\ * & 0 & * \\ * & * & 0 \end{bmatrix} \tag{19}$$

For the virtual uniaxial tensile tests along different directions θ, the Euler orientations in all grains are rotated as $[\phi_1 - \theta, \Phi, \phi_2]$ but also the grain geometries are rotated θ degree about ND axis to take account for the effect of grain morphology. Fig. 18a and b show the distribution of the true stress and true strain in the deformed DP780 RVE in the virtual tensile tests aligned with RD at the stage of the macroscopic plastic strain with 0.1. The phase boundary between the martensite and ferrite phases in the RVE is plotted using the black solid line. The full-field CP simulations show the strength of the martensite phase is significantly higher than the ferrite phases, and the crystalline slips mainly occur in the ferrite phases. The variation of the true stress and strain through a line in the RVE (indicated in Fig. 18b) are illustrated in Fig. 18c. The true stress with about 1.5 GPa is observed in the martensite phase, while that is about 0.6 GPa in the ferrite phase. The true strain distribution in the martensite phase is from 0.02 to 0.06, while that is at a range of 0.05 to 0.16 in the ferrite phase. Therefore, the hard martensite phase significantly improves the strength of the DP steel, but it obstructs the continuous slip in the ferrite phase, and thus reduces the elongation.

The distribution of the true stress and true strain in the deformed DP980 RVE in the virtual tensile tests aligned with RD with a macroscopic plastic train of 0.05 are illustrated in Fig. 19a and b, respectively. Due to the higher volume fraction of the martensite phase compared with DP780, the yield stress and UTS of the DP980 are further improved, but the continuous slip of the soft ferrite phase is more difficult, which further reduces the elongation of DP steel. Fig. 19c shows the distribution of the true stress and strain through the line in RVE (indicated in Fig. 19b). It is seen that the variation of the true stress and strain significantly fluctuate through the mixed hard martensite and soft ferrite phase.

In addition, the virtual uniaxial tensile tests aligned with various angles from RD to TD at an interval of 5° for the DP780 and DP980 were conducted to obtain the directional normalized yield stress and r-value. Here, rotating the Euler angle of the grain orientation is utilized as an equivalent method for rotating the loading direction. Following the Euler angles Bunge notation, the grain orientation in-plane rotation from rolling direction (RD) to transfers direction (TD) at angle ϕ as $[\phi_1\text{-}\phi, \Phi, \phi_2]$. The comparison of the directional normalized yield stress and r-value obtained from experimental and virtual uniaxial tests for the DP780 and DP980 are illustrated in Fig. 20a and b, respectively. Since the crystalline morphology, texture and phase fraction of the RVE used in the virtual tests is approximately identical to the realistic microstructure observed in the DP780 and DP980, a good agreement of the uniaxial plastic anisotropy is obtained between the experiments and virtual tests for both the DP780 and DP980.

The virtual biaxial tensile tests with stress ratio of $\sigma_{11} : \sigma_{22} = 1:1$ are performed using the DP780 RVE, and corresponding distribution of the Mises equivalent stress and strain in the deformed RVE at the stage of macroscopic equivalent strain with 0.1 are shown in Fig. 21a and b, respectively. In the biaxial stress state, the martensite phase shows relatively high strength and low plastic deformation level that is contrary to the ferrite phase. Fig. 21c shows that the Mises equivalent stress is about 2 GPa and 0.8 GPa
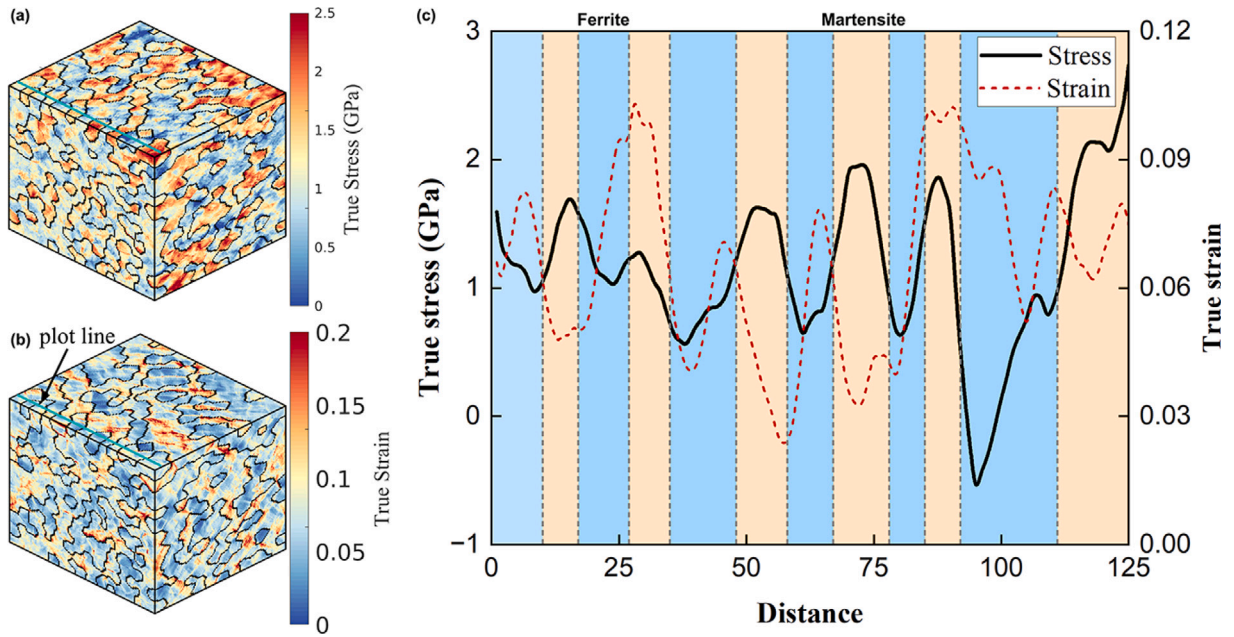
Fig. 19. (a) The distribution of true stress along the loading direction on the deformed RVE of DP980 at equivalent plastic strain of 0.05; (b) The distribution of true strain along the loading direction on the deformed RVE of DP980 aan t equivalent plastic strain of 0.05; (c) The variation of the true stress and strain in the mixed ferrite and martensite phase through the plot line.

Table 2
The parameters of the modified YU model for the dual phase steels.

Degradation of elastic modulus							
	E_0 (GPa)	E_a (GPa)	ξ		E_0 (GPa)	E_a (GPa)	ξ
CP. DP780:	205.49	158.86	78.98	EXP. DP780:	207.13	157.42	75.78
CP. DP980:	212.31	165.02	99.83	EXP. DP980:	213.31	165.83	84.95
Kinematic hardening model							
	y (MPa)	b_0 (MPa)	γ_1	c_2 (MPa)	γ_2	Q (MPa)	b
CP. DP780, EXP.DP780:	395.2	586.3	20.5	305.2	110.3	55.3	105.8
CP. DP980, EXP.DP980:	585.2	926.3	21.5	355.2	100.3	55.3	45.8

in the martensite and ferrite phase through the plot line in RVE, and the Mises equivalent strain in the martensite phase is lower than in ferrite phase. Fig. 22a and b respectively plot the distribution of the Mises equivalent stress and strain in the deformed RVE of DP980 with 0.05 macroscopic equivalent strain, where the high volume fraction of martensite phase also significantly improves the biaxial strength but results in difficulty of plastic deformation of dual phase steel. Fig. 22c shows the variation of the Mises equivalent stress fluctuates through the intertwined hard martensite and soft ferrite phase.

The virtual biaxial tensile tests with various stress ratios are performed to predict the yield locus at different equivalent plastic strain levels. Fig. 23a and b show the comparison of the yield locus at different equivalent plastic strains obtained from the experimental and virtual biaxial tensile tests for DP780 and DP980, respectively. It can be seen that the virtual biaxial tensile tests successfully predict the evolution of the yield locus in the RD-TD plane for both DP780 and DP980 at various equivalent plastic strain levels due to the well-designed strategy for synthetic microstructure generation and crystal plasticity parameter calibration.

In summary, the virtual testing results show the full-field CP modelling using the appropriate RVEs, which take account for the actual grain morphology, texture and phase distribution, could be a substitute approach for the complicated physical tests in the characterization of uniaxial and biaxial anisotropic plasticity of dual phase steel.

5.3. The calibration of the experimental and virtual tests based constitutive model

In this section, the calibration of the yield function and kinematic hardening model are conducted using the results of the experimental and virtual mechanical tests. Accordingly, two advanced constitutive models, i.e. the experimental and virtual tests based constitutive models are established to perform the sheet metal forming simulations.
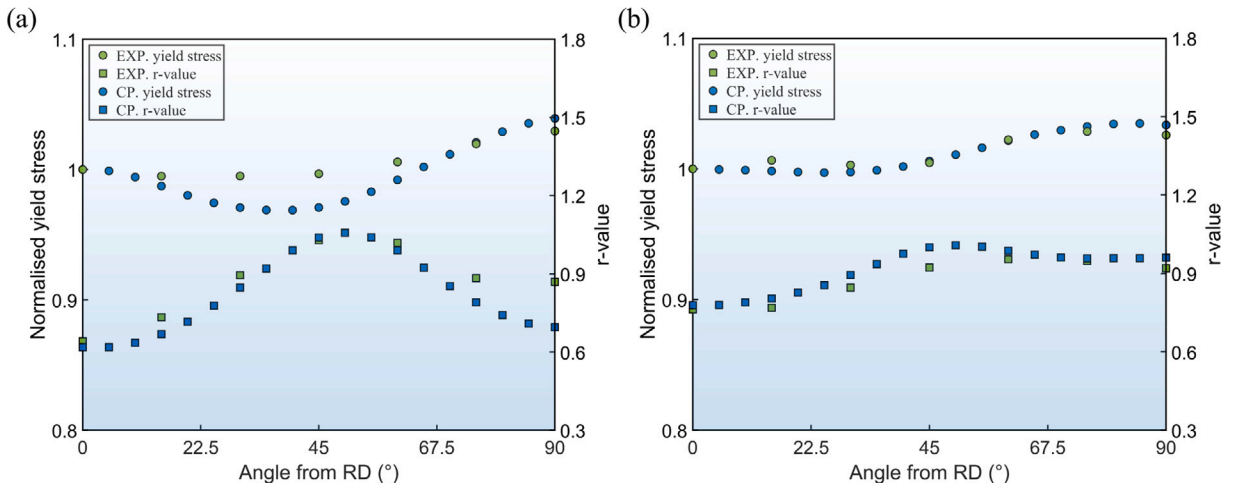
Fig. 20. The variation of the uniaxial normalized yield stress and r-value from the RD to TD at an interval of 5° predicted by the virtual tests by comparison with the experimental data at an interval of 15° for (a) DP780 at equivalent plastic strain of 1.5% and (b) DP980 at equivalent plastic strain of 0.7%.
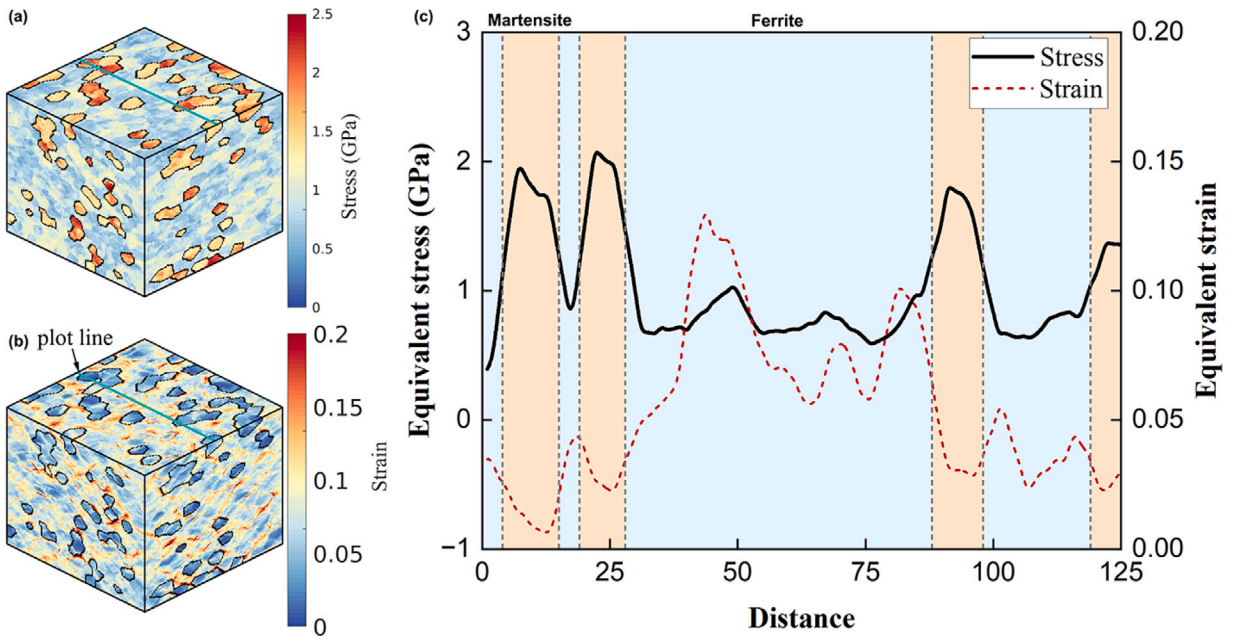

Fig. 21. (a) The distribution of Mises equivalent stress on the deformed RVE of DP780 at an equivalent plastic strain of 0.1; (b) The distribution of Mises equivalent plastic strain on the deformed RVE of DP780 at equivalent plastic strain of 0.1; (c) The variation of the Mises equivalent stress and strain in the mixed ferrite and martensite phase through the line indicated in Fig. 15b.

5.4. The calibration of the YU model

During the draw-bending process in the U-bending test, the reverse tension–compression deformation occurs in the sheet metal when the material goes through the tool radius. Therefore, the kinematic hardening behaviour in the reverse tension–compression loading should be taken into account in the constitutive models to obtain accurate plastic deformation and springback prediction. Therefore, the stress–strain curves in reverse tension–compression loading stated above are utilized to calibrate the parameters of the modified YU models, which are documented in Table 2. As illustrated in Fig. 24a–d, these calibrated modified YU models successfully reproduce the cyclic stress–strain curves for both DP780 and DP980 obtained by experiments and virtual tests with various prestrain levels.
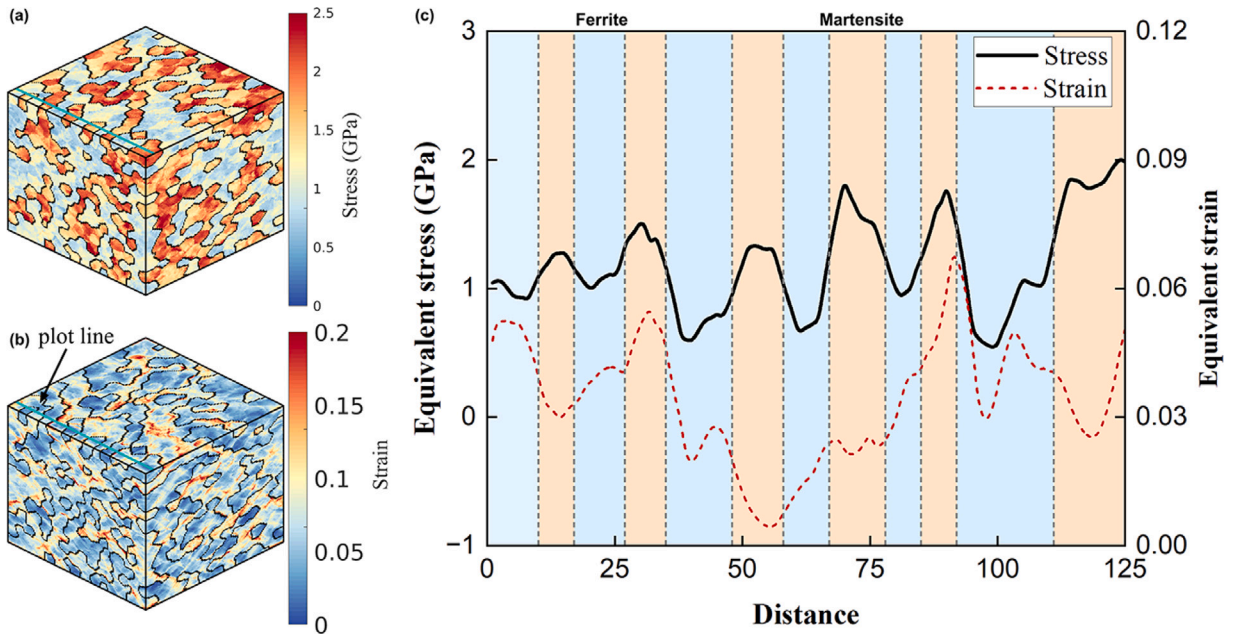
Fig. 22. (a) The distribution of Mises equivalent stress on the deformed RVE of DP980 at an equivalent plastic strain of 0.05; (b) The distribution of Mises equivalent plastic strain on the deformed RVE of DP980 at equivalent plastic strain of 0.05; (c) The variation of the Mises equivalent stress and strain in the mixed ferrite and martensite phase through the line indicated in Fig. 16b.
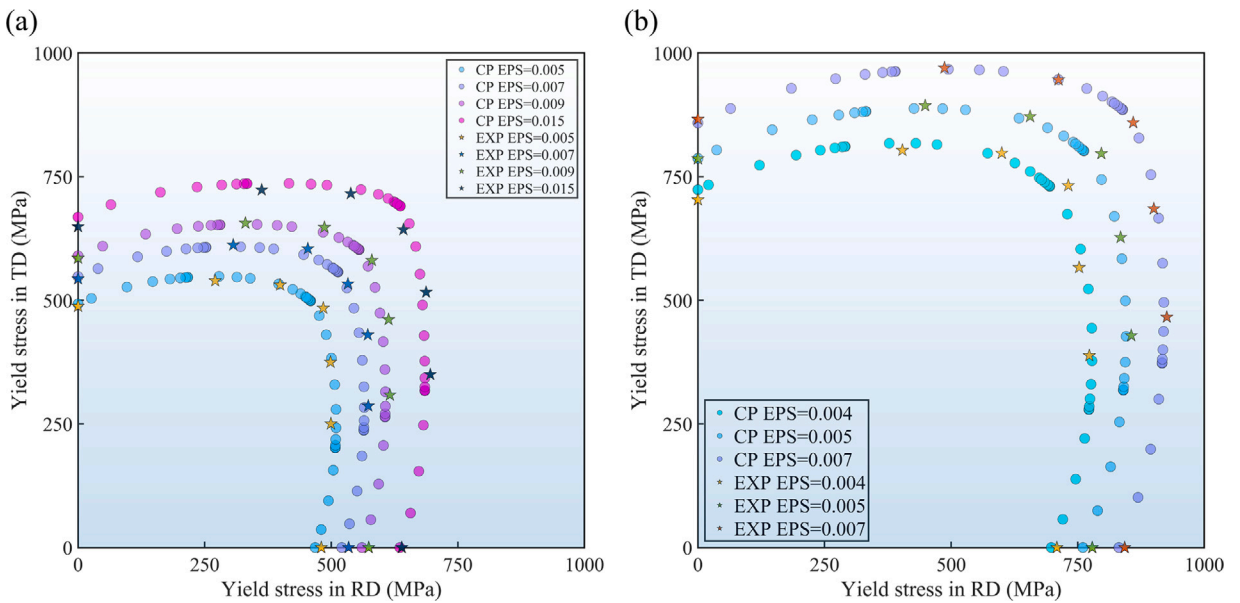

Fig. 23. The biaxial yield stress with various stress ratios in RD-TD plane predicted by the virtual tests by comparison with the experimental data obtained by the physical biaxial tensile tests for (a) DP780 at equivalent plastic strain from 0.5% to 1.5% and (b) DP980 at equivalent plastic strain from 0.4% to 0.7%.

5.5. The calibration of the yield function

The uniaxial and biaxial plastic anisotropy obtained by experiments and virtual tests illustrated in Fig. 20 are utilized to calibrate the Yld2004-18p yield function so-called EXP. Yld2004-18p and CP. Yld2004-18p, respectively. Additionally, the experimental and virtual tests are also used to calibrate Yld2000-2d yield function so-called EXP. Yld2000-2d and CP. Yld2000-2d, respectively. The well-known non-linear least-square method Levenberg–Marquardt algorithm was applied to determine the anisotropic coefficients of the yield function curve so that the sum of the squares of the deviations between the plastic anisotropy data and calculation is
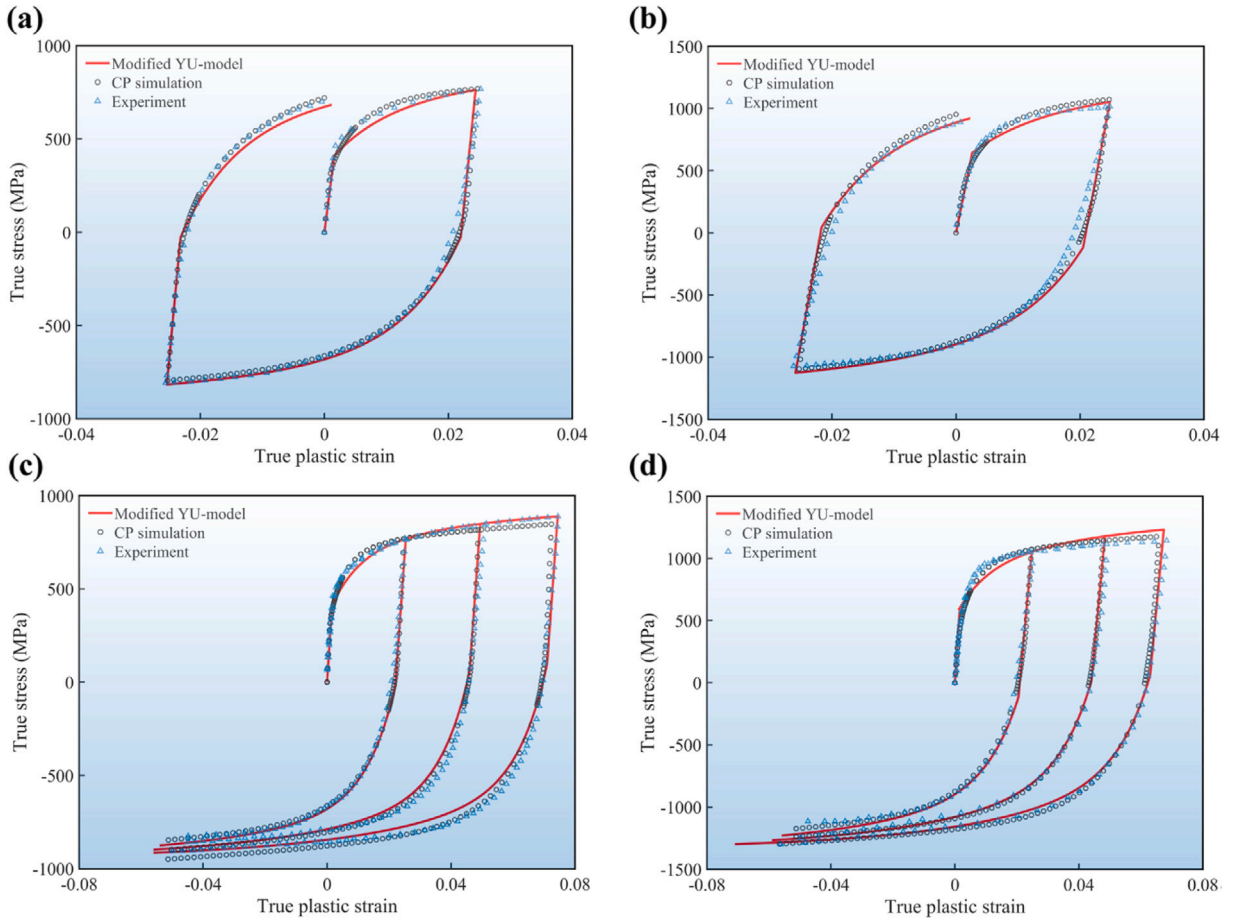
Fig. 24. The true stress versus true strain curves in the 1.5 cycles of uniaxial tension and reverse compression loading obtained by the experiment, virtual test and calibrated modified YU model for (a) DP780 and (b) DP980; The true stress versus true strain response in three groups of uniaxial tension and reverse compression loading with various prestrain levels obtained by the experiments, virtual tests and calibrated modified YU model for (c) DP780 and (d) DP980.

Table 3
The parameters of Yld2000-2d model for DP780 and DP980 calibrated by experimental data (exponent a = 8).

DP780:							
α_1	α_2	α_3	α_4	α_5	α_6	α_7	α_8
0.984148	0.939226	0.909245	0.968794	1.015997	0.993747	1.003265	1.033796
DP980:							
α_1	α_2	α_3	α_4	α_5	α_6	α_7	α_8
1.004921	0.932126	0.887137	0.959935	1.009918	1.001819	0.981834	1.025638

minimized. The details of the fitting numerical procedure see Ref. Liu et al. (2020a). The optimized parameters of the Yld2004-18p yield functions are documented in Tables 5 and 6, and parameters of Yld2000-2d yield functions are summarized in Tables 3 and 4.

For the DP780, the prediction of Exp. Yld2004-18p, CP. Yld2004-18p, Exp. Yld2000-2d and CP. Yld2000-2d for the variation of the normalized yield stress and r-values and for the yield locus in RD-TD plane are illustrated in Fig. 25a and b, respectively. Similarly, these data of DP980 are also shown in Fig. 25c and d. It can be seen that all of the Exp. Yld2004-18p, CP. Yld2004-18p, Exp. Yld2000-2d and CP. Yld2000-2d could accurately capture the corresponding input plastic anisotropy for calibration in dual phase steels. These calibrated yield functions are implemented into the FE subroutine code to predict the plastic deformation and springback of DP780 and DP980 in the U-bending simulations.

6. U-bending springback prediction

To compare the accuracy of the virtual tests and physical tests calibrated constitutive models in the prediction of springback for dual phase steels, the U-bending simulations are conducted using the Exp. Yld2004-18p, CP. Yld2004-18p, Exp. Yld2000-2d
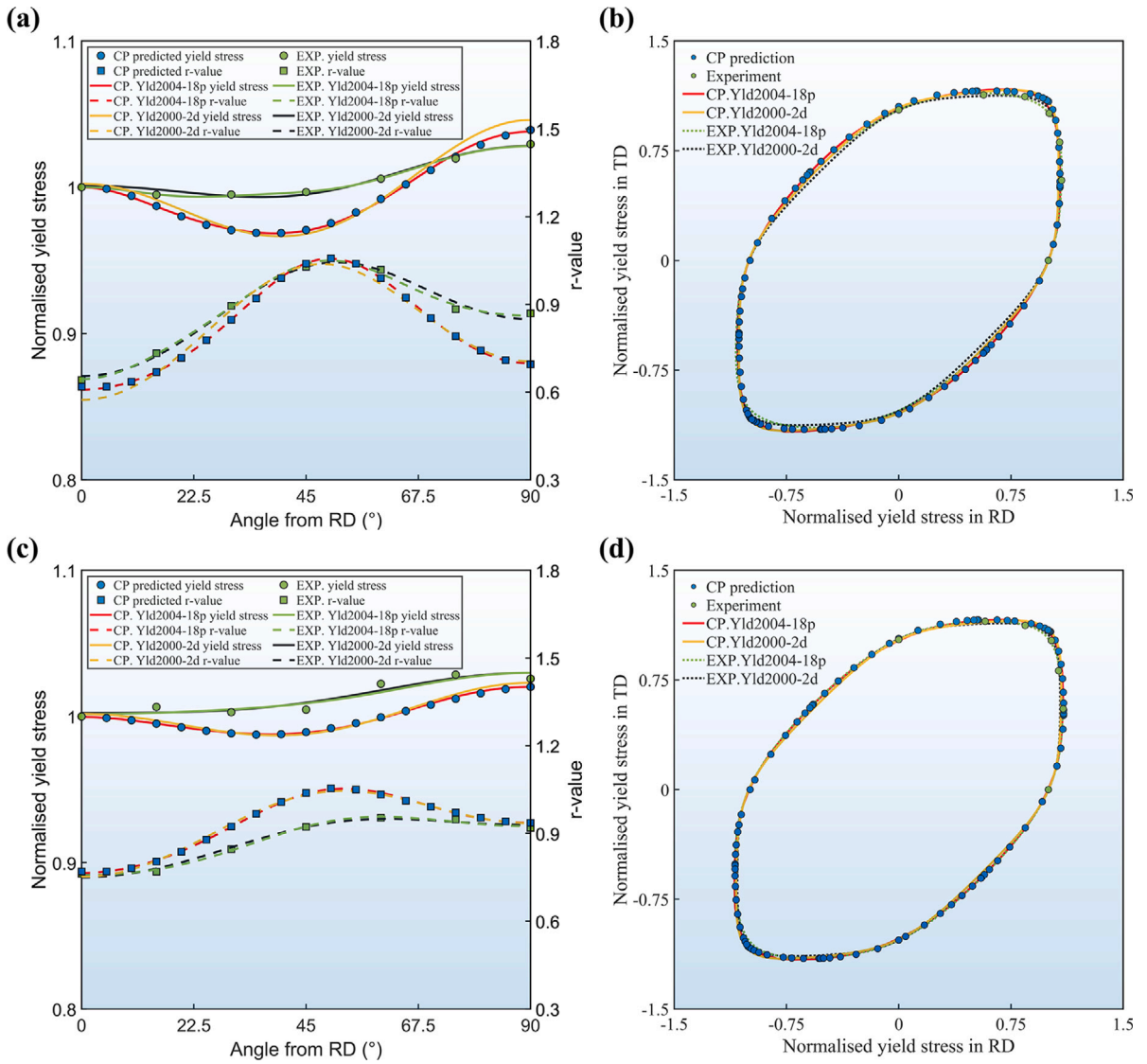
(a)

(b)

(c)

(d)

Fig. 25. The r-value and normalized yield stress versus uniaxial tension direction of the (a) DP780 and (c) DP980 obtained by (i) the physical uniaxial tensile test, EXP.Yld2004-18p and EXP. Yld2000-2d yield function, and by (ii) the virtual test, CP. Yld2004-18p and CP. Yld2000-2d yield function. The yield surface in RD-TD of the (b) DP780 and (d) DP980 obtained by (i) the physical biaxial tensile test, EXP.Yld2004-18p and EXP. Yld2000-2d yield function, and by (ii) the virtual test, CP. Yld2004-18p and CP. Yld2000-2d yield function.

Table 4
The parameters of Yld2000-2d model for DP780 and DP980 calibrated by virtual tests data (exponent a = 8).

DP780:							
α_1	α_2	α_3	α_4	α_5	α_6	α_7	α_8
1.025284	0.846006	0.794255	0.943048	1.021203	1.013578	1.023618	1.124429
DP980:							
α_1	α_2	α_3	α_4	α_5	α_6	α_7	α_8
1.000804	0.935300	0.819359	0.951249	1.005607	0.976891	1.005467	1.084366

and CP. Yld2000-2d model, respectively. The degradation elastic modulus, kinematic hardening and plastic anisotropy predicted by full-field CP simulations are taken into account in the CP. Yld2004-18p and CP. Yld2000-2d model. These properties obtained by the experimental tests are also considered by the EXP. Yld2000-2d and Exp. Yld2004-18p model. The configuration of the specimens after springback obtained from the experiments and the equivalent plastic strain distribution of the specimens after springback predicted by the Exp. Yld2004-18p, CP. Yld2004-18p, Exp. Yld2000-2d and CP. Yld2000-2d model model for DP780 and DP980 are

Table 5

The parameters of Yld2004-18 model for DP780 and DP980 calibrated by experimental tests (exponent a = 8).

DP780:

α_1	α_2	α_3	α_4	α_5	α_6	α_7	α_8	α_9
1.201617	1.117322	0.718502	0.897208	1.113564	0.190301	1.000000	1.000000	0.893370
α_{10}	α_{11}	α_{12}	α_{13}	α_{14}	α_{15}	α_{16}	α_{17}	α_{18}
0.868515	0.076203	0.663262	0.731499	1.062559	1.125348	1.000000	1.000000	1.024921

DP980:

α_1	α_2	α_3	α_4	α_5	α_6	α_7	α_8	α_9
1.175031	1.200361	0.845920	0.903277	1.035893	0.638312	1.000000	1.000000	1.018284
α_{10}	α_{11}	α_{12}	α_{13}	α_{14}	α_{15}	α_{16}	α_{17}	α_{18}
0.978779	0.533994	0.743485	0.688480	0.949982	1.148073	1.000000	1.000000	0.903667

Table 6

The parameters of Yld2004-18 model for DP780 and DP980 calibrated by virtual tests (exponent a = 8).

DP780:

α_1	α_2	α_3	α_4	α_5	α_6	α_7	α_8	α_9
1.328759	1.325396	0.829447	0.874804	1.199931	0.399428	1.737090	−0.004733	1.094483
α_{10}	α_{11}	α_{12}	α_{13}	α_{14}	α_{15}	α_{16}	α_{17}	α_{18}
0.812237	0.270006	0.532485	0.739469	0.857707	1.147123	−0.012249	1.655786	0.901675

DP980:

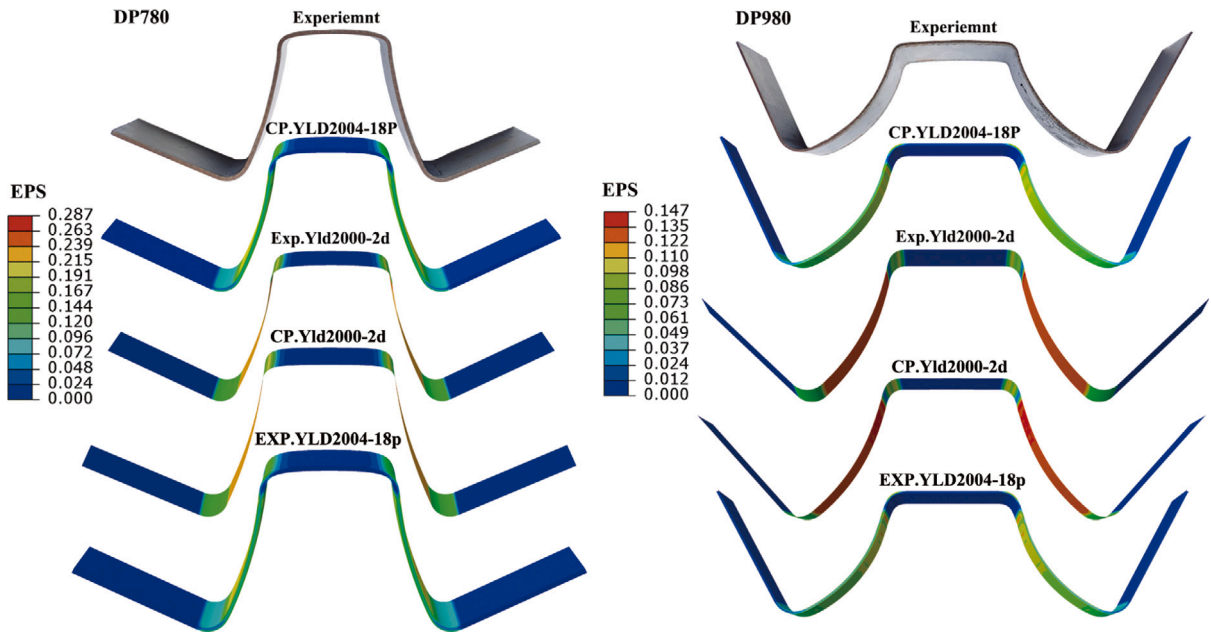| α_1	α_2	α_3	α_4	α_5	α_6	α_7	α_8	α_9
1.243594	1.175831	0.839433	0.875971	1.064991	0.351067	1.728406	0.541875	1.032635
α_{10}	α_{11}	α_{12}	α_{13}	α_{14}	α_{15}	α_{16}	α_{17}	α_{18}
0.873466	0.222209	0.707425	0.701954	0.984650	1.146146	0.072471	1.362499	0.918230

Fig. 26. The Exp. Yld2004-18p, CP. Yld2004-18p, Exp. Yld2000-2d and CP. Yld2000-2d models predicted configuration of the U-shaped parts with equivalent plastic strain distribution after springback compared with experimental specimens for (a) DP780 and (b) DP980.

illustrated in Fig. 26a and b, respectively. It is seen that the prediction of equivalent plastic strain in the drawing area obtained by EXP. Yld2000-2d and CP. Yld2000-2d model is higher than Exp. Yld2004-18p and CP. Yld2004-18p model due to the difference in solid and shell elements with respect to the stress integration method in the thickness direction.

The profile of the experimental specimen after springback is measured which is used to verify the prediction of the Exp. Yld2004-18p, CP. Yld2004-18p, Exp. Yld2000-2d and CP. Yld2000-2d models. Fig. 27a shows the predictions of CP. Yld2004-18p, CP. Yld2000-2d and Exp. Yld2004-18p are in good agreement with the experimental DP780 specimen profile after springback, and EXP. Yld2000-2d model slightly overestimated the springback level. For the DP980 specimen, both of the CP.Yld2004-18p and EXP.Yld2004-18p models can give an accurate profile prediction in comparison with the experiments, while the results provided
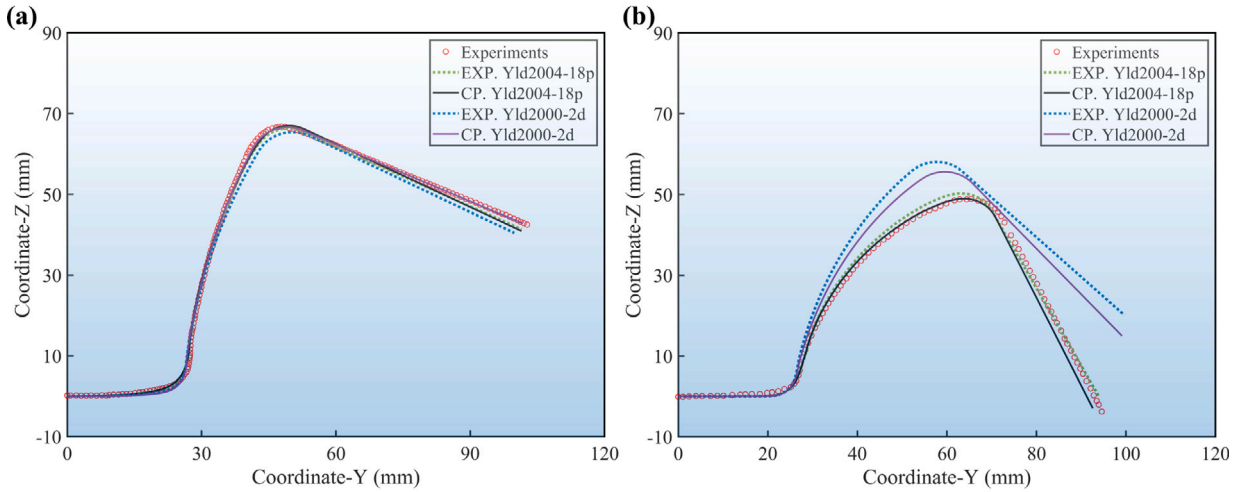
(a)

(b)

Fig. 27. The profiles of the U-shaped parts after springback measured by experiments and predicted by Exp. Yld2004-18p, CP. Yld2004-18p, Exp. Yld2000-2d and CP. Yld2000-2d models for (a) DP780 and (b) DP980.
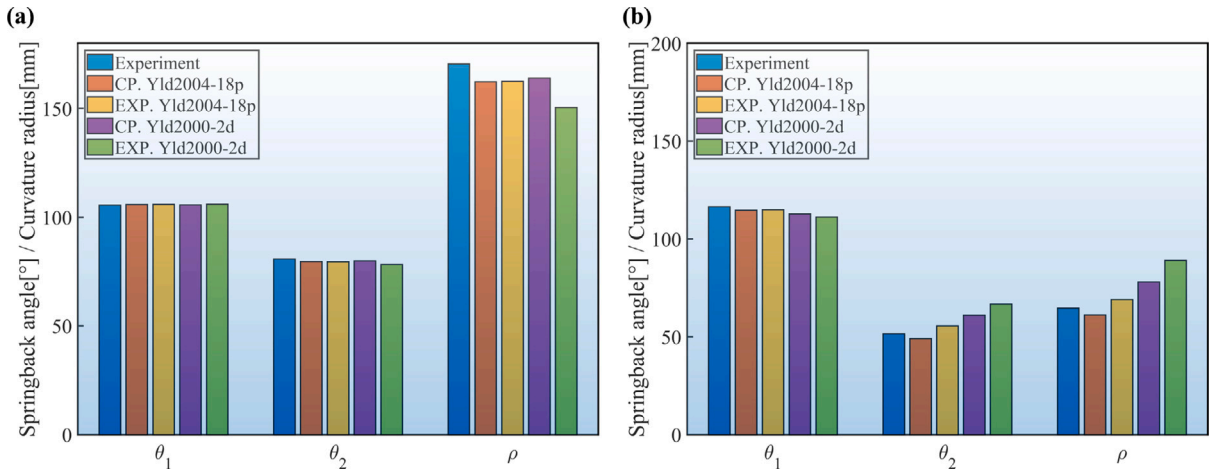
(a)

(b)

Fig. 28. The springback angles θ_1 and θ_2 and curvature radius ρ of the U-shaped parts measured by experiments and predicted by Exp. Yld2004-18p, CP. Yld2004-18p, Exp. Yld2000-2d and CP. Yld2000-2d models for (a) DP780 and (b) DP980.

by the CP. Yld2000-2d and EXP. Yld2000-2d models are significantly underestimated as illustrated in Fig. 27b. The springback angle θ_1, θ_2 and curvature radius ρ of DP780 and DP980 obtained from experimental specimens and predicted by various models are compared and shown in Fig. 28a and b, respectively. To quantify the accuracy of simulations, the root mean square deviation (RMSD) for the springback angles and curvature radius is calculated by,

$$\text{RMSD} = \sqrt{\frac{1}{3}\left[\left(\frac{\theta_1^{\text{pre}}}{\theta_1^{\text{exp}}} - 1\right)^2 + \left(\frac{\theta_2^{\text{pre}}}{\theta_2^{\text{exp}}} - 1\right)^2 + \left(\frac{\rho^{\text{pre}}}{\rho^{\text{exp}}} - 1\right)^2\right]} \tag{20}$$

where the superscript "pre" and "exp" denote the prediction of simulation and experimental results.

The RMSD of CP. Yld2004-18p, Exp. Yld2000-2d, CP. Yld2000-2d and Exp. Yld2004-18p models for DP780 are 2.92%, 7.02%, 2.29% and 2.88%, respectively. These RMSD values of DP980 are 4.27%, 27.74%, 16.08% and 5.94%, respectively. The advanced constitutive model consisting of Yld2004-18p yield function and modified YU model calibrated by extensive experimentally mechanical tests, including ULUL, directional uniaxial tensile tests, cyclic tension–compression tests and biaxial tensile tests, show a good performance in prediction of springback for various DP steels. These physical tests require costly experimental equipment like biaxial tensile machines and 3D-DIC systems, complex specimen designs and experimental procedures, and complicated post-data analysis. Meanwhile, the virtual tests, in which the parameters are only calibrated by cyclic tension–compression tests, successfully reproduced these experimental tests. The advanced phenomenological constitutive model calibrated by the virtual tests also shows a good performance in the prediction of springback for both DP780 and DP980. Therefore, the results show that the virtual tests

could be an appropriate substitute for the elaborated extensive physical tests for complex elastic behaviour, path-dependent strain hardening behaviour and plastic anisotropy in complicated stress states that are difficult to obtain by physical experiments. Since the property information of in-plane plastic anisotropy, kinematic hardening behaviour and degradation of elastic modulus used in the calibration of these various models is similar, the higher deviation in the prediction of Exp. Yld2000-2d and CP. Yld2000-2d model for the thin DP980 sheets using shell elements may be attributed to that without consideration of the out-of-plane mechanical behaviour. For instance, when the sheet metal passes over a tool radius, the material is subjected to tension deformation on the outside surface and that is relatively low compression on the inside surface over the sheet thickness direction. This is taken into account in the Yld2004-18p model but not in Yld2000-2d model.

It should be noted that the calibration of the full-field multi-phase CP model only used the experimental stress–strain curves in tension–compression–tension tests of DP780 and DP980. The calibrated CP model only used one set of parameters for martensite and ferrite phases show a good performance in the prediction of kinematic hardening, elastic modules degradation and plastic anisotropy for different DP steels with different thicknesses. Therefore, the virtual tests based on the full-field multi-phase CP model with mixed isotropic and kinematic hardening could be an accurate approach to calibrate the advanced phenomenological constitutive model and thus accurately predict the mechanical behaviour of high-strength DP steels in forming processes.

7. Conclusions

In this research, a virtual multi-scale laboratory enabled constitutive framework for describing the complex deformation responses of dual phase steels is proposed, implemented, verified and validated in practical forming processes. The virtual laboratory is developed based on multi-phase, full-field crystal plasticity (CP) modelling, in which, particularly, the evolution of dislocation density induced strain hardening, dislocation pile-up-induced kinematic hardening and degradation of elastic modulus are carefully taken into account for improved capability for virtual characterization of complex deformation behaviours. Using two DP steels i.e., DP780 and DP980, as case materials, the plastic anisotropy, kinematic hardening behaviours, and nonlinear elastic modulus degradation are investigated by the experimental tests and full-field crystal plasticity modelling based virtual tests including the directional uniaxial tensile tests, biaxial tensile tests and reverse tension–compression tests. The high resolution 3D RVEs for the virtual tests of dual phase steels are carefully generated with a synthetic microstructure, which is approximately identical to the experimentally characterized microstructures including the phase distribution, volume fraction of martensite and ferrite phase, grain shape and texture. With respect to the macroscale plastic anisotropy such as variation of uniaxial normalized yield stress, r-value and biaxial yield locus, a good agreement with the experiments is achieved in the CP-based virtual tests. Additionally, the kinematic hardening behaviour during the reverse tension–compression loading, as well as deformation-induced elastic modulus degradation is successfully predicted by the virtual tests. In addition, the micromechanical response of DP steels such as the inhomogeneity of the stress and strain distribution in the mixed ferrite and martensite phases are successfully captured by the multi-phase crystal plasticity modelling.

For improving the analysis of DP steel forming processes, two phenomenological constitutive models are employed and calibrated, including the experimentally calibrated in-plane Yld2000-2d and virtually calibrated 3D Yld2004-18p yield functions, associated with the modified YU kinematic hardening model. By using the models in the analysis of deformation and springback behaviours in the U-bending process of DP780 and DP980 sheets, the prediction capabilities of the different models and calibration methods are assessed. It is found that the virtual tests calibrated constitutive model shows good performance in terms of the prediction in springback by comparison with experiments. Therefore, the virtual tests calibrated constitutive models could be a useful approach utilized to provide accurate simulation and analysis of sheet metal forming processes for advanced metal materials with complex microstructures. The findings support that the virtual laboratory enabled modelling approach provides a substitute for the costly mechanical tests, in particular for some hard-to-access physical tests that are required in the calibration of advanced constitutive models, thereby contributing to a more reliable, efficient, and cost-effective analysis of sheet forming processes.

CRediT authorship contribution statement

Wencheng Liu: Writing – original draft, Validation, Methodology, Investigation, Conceptualization. **Xinghao Li:** Validation, Investigation. **Ming Liu:** Visualization, Investigation. **Hao Cui:** Resources, Investigation. **Jia Huang:** Resources, Formal analysis. **Yong Pang:** Validation, Investigation. **Jun Ma:** Writing – review & editing, Writing – original draft, Supervision, Methodology, Investigation.

Declaration of competing interest

Data availability

Data will be made available on request.

Acknowledgements

References

Amirmaleki, M., Samei, J., Green, D.E., Van Riemsdijk, I., Stewart, L., 2016. 3D micromechanical modeling of dual phase steels using the representative volume element method. Mech. Mater. 101, 27–39.

Balan, T., Lemoine, X., Maire, E., Habraken, A.-M., 2015. Implementation of a damage evolution law for dual-phase steels in Gurson-type models. Mater. Des. 88, 1213–1222.

Barlat, F., Aretz, H., Yoon, J., Karabin, M., Brem, J., Dick, R., 2005. Linear transfomation-based anisotropic yield functions. Int. J. Plast. 21 (5), 1009–1039.

Barlat, F., Brem, J., Yoon, J., Chung, K., Dick, R., Lege, D., Pourboghrat, F., Choi, S.-H., Chu, E., 2003. Plane stress yield function for aluminum alloy sheets—part 1: theory. Int. J. Plast. 19 (9), 1297–1319.

Barlat, F., Ha, J., Grácio, J.J., Lee, M.-G., Rauch, E.F., Vincze, G., 2013. Extension of homogeneous anisotropic hardening model to cross-loading with latent effects. Int. J. Plast. 46, 130–142.

Barlat, F., Vincze, G., Grácio, J., Lee, M.-G., Rauch, E., Tomé, C., 2014. Enhancements of homogenous anisotropic hardening model and application to mild and dual-phase steels. Int. J. Plast. 58, 201–218.

Barrett, T.J., Knezevic, M., 2019. Deep drawing simulations using the finite element method embedding a multi-level crystal plasticity constitutive law: Experimental verification and sensitivity analysis. Comput. Methods Appl. Mech. Engrg. 354, 245–270.

Bong, H.J., Hu, X., Sun, X., Ren, Y., 2019a. Mechanism-based constitutive modeling of ZEK100 magnesium alloy with crystal plasticity and in-situ HEXRD experiment. Int. J. Plast. 113, 35–51.

Bong, H.J., Lee, J., 2021. Crystal plasticity finite element–Marciniak-Kuczynski approach with surface roughening effect in predicting formability of ultra-thin ferritic stainless steel sheets. Int. J. Mech. Sci. 191, 106066.

Bong, H.J., Lee, J., Lee, M.-G., Kim, D., 2019b. Identification of mechanical responses of steel sheets under non-proportional loadings using dislocation-density based crystal plasticity model. Int. J. Mech. Sci. 155, 461–474.

Bong, H.J., Lim, H., Lee, M.-G., Fullwood, D.T., Homer, E.R., Wagoner, R.H., 2017. An RVE procedure for micromechanical prediction of mechanical behavior of dual-phase steel. Mater. Sci. Eng. A 695, 101–111.

Cantara, A.M., Zecevic, M., Eghtesad, A., Poulin, C.M., Knezevic, M., 2019. Predicting elastic anisotropy of dual-phase steels based on crystal mechanics and microstructure. Int. J. Mech. Sci. 151, 639–649.

Chaboche, J.-L., 2008. A review of some plasticity and viscoplasticity constitutive theories. Int. J. Plast. 24 (10), 1642–1693.

Choi, S.-H., Kim, E.-Y., Woo, W., Han, S., Kwak, J., 2013. The effect of crystallographic orientation on the micromechanical deformation and failure behaviors of DP980 steel during uniaxial tension. Int. J. Plast. 45, 85–102.

Choi, J., Lee, J., Bae, G., Barlat, F., Lee, M.-G., 2016. Evaluation of springback for DP980 S rail using anisotropic Hardening models. JOM 68 (7), 1850–1857.

Choi, J., Lee, J., Bong, H.J., Lee, M.-G., Barlat, F., 2018. Advanced constitutive modeling of advanced high strength steel sheets for springback prediction after double stage U-draw bending. Int. J. Solids Struct. 151, 152–164.

Daroju, S., Kuwabara, T., Knezevic, M., 2022. Experimental characterization and crystal plasticity modeling of dual-phase steels subjected to strain path reversals. Mech. Mater. 168, 104293.

Deng, N., Korkolis, Y.P., 2018. Elastic anisotropy of dual-phase steels with varying martensite content. Int. J. Solids Struct. 141, 264–278.

Deng, N., Kuwabara, T., Korkolis, Y., 2015. Cruciform specimen design and verification for constitutive identification of anisotropic sheets. Exp. Mech. 55, 1005–1022.

Deng, N., Kuwabara, T., Korkolis, Y.P., 2018. On the non-linear unloading behavior of a biaxially loaded dual-phase steel sheet. Int. J. Mech. Sci. 138, 383–397.

Diehl, M., An, D., Shanthraj, P., Zaefferer, S., Roters, F., Raabe, D., 2017. Crystal plasticity study on stress and strain partitioning in a measured 3D dual phase steel microstructure. Phys. Mesomech. 20, 311–323.

Ebrahimi, F., Saeidi, N., Raeissi, M., 2020. Microstructural modifications of Dual-Phase steels: An overview of recent progress and challenges. Steel Res. Int. 91 (10), 2000178.

Eghtesad, A., Knezevic, M., 2020. High-performance full-field crystal plasticity with dislocation-based hardening and slip system back-stress laws: Application to modeling deformation of dual-phase steels. J. Mech. Phys. Solids 134, 103750.

Eisenlohr, P., Diehl, M., Lebensohn, R., Roters, F., 2013. A spectral method solution to crystal elasto-viscoplasticity at finite strains. Int. J. Plast. 46, 37–53.

Esmaeilpour, R., Kim, H., Park, T., Pourboghrat, F., Xu, Z., Mohammed, B., Abu-Farha, F., 2018. Calibration of Barlat Yld2004-18P yield function using CPFEM and 3D RVE for the simulation of single point incremental forming (SPIF) of 7075-O aluminum sheet. Int. J. Mech. Sci. 145, 24–41.

Fansi, J., Balan, T., Lemoine, X., Maire, E., Landron, C., Bouaziz, O., Bettaieb, M.B., Habraken, A.M., 2013. Numerical investigation and experimental validation of physically based advanced GTN model for DP steels. Mater. Sci. Eng. A 569, 1–12.

Feng, Z., Li, H., Zhang, D., Guo, X., Chen, Y., Fu, M., 2022. Multi-aspect size effect transition from micro to macroscale: Modelling and experiment. Int. J. Plast. 156, 103364.

Feng, Z., Yoon, S.-Y., Choi, J.-H., Barrett, T.J., Zecevic, M., Barlat, F., Knezevic, M., 2020. A comparative study between elasto-plastic self-consistent crystal plasticity and anisotropic yield function with distortional hardening formulations for sheet metal forming. Mech. Mater. 148, 103422.

Gawad, J., Banabic, D., Van Bael, A., Comsa, D.S., Gologanu, M., Eyckens, P., Van Houtte, P., Roose, D., 2015. An evolving plane stress yield criterion based on crystal plasticity virtual experiments. Int. J. Plast. 75, 141–169.

Ghaei, A., Taherizadeh, A., 2015. A two-surface hardening plasticity model based on non-associated flow rule for anisotropic metals subjected to cyclic loading. Int. J. Mech. Sci. 92, 24–34.

Ha, J., Lee, J., Kim, J.H., Lee, M.-G., Barlat, F., 2017. Investigation of plastic strain rate under strain path changes in dual-phase steel using microstructure-based modeling. Int. J. Plast. 93, 89–111.

Hanabusa, Y., Takizawa, H., Kuwabara, T., 2013. Numerical verification of a biaxial tensile test method using a cruciform specimen. J. Mater Process. Technol. 213 (6), 961–970.

Hérault, D., Thuillier, S., Lee, S.-Y., Manach, P.-Y., Barlat, F., 2021. Calibration of a strain path change model for a dual phase steel. Int. J. Mech. Sci. 194, 106217.

Hou, Y., Min, J., Guo, N., Lin, J., Carsley, J.E., Stoughton, T.B., Traphöner, H., Clausmeyer, T., Tekkaya, A.E., 2019. Investigation of evolving yield surfaces of dual-phase steels. J. Mater Process. Technol. 116314.

Hou, Y., Min, J., Guo, N., Shen, Y., Lin, J., 2021. Evolving asymmetric yield surfaces of quenching and partitioning steels: Characterization and modeling. J. Mater Process. Technol. 290, 116979.

Jeong, Y., Barlat, F., Tomé, C.N., Wen, W., 2017. A comparative study between micro- and macro-mechanical constitutive models developed for complex loading scenarios. Int. J. Plast. 93, 212–228.

Jeong, Y., Jeon, B., Tomé, C.N., 2021. Finite element analysis using an incremental elasto-visco-plastic self-consistent polycrystal model: FE simulations on Zr and low-carbon steel subjected to bending, stress-relaxation, and unloading. Int. J. Plast. 147, 103110.

Joo, M., Wi, M.-S., Yoon, S.-Y., Lee, S.-Y., Barlat, F., Tomé, C.N., Jeon, B., Jeong, Y., 2023. A crystal plasticity finite element analysis on the effect of prestrain on springback. Int. J. Mech. Sci. 237, 107796.

Kim, H., Barlat, F., Lee, Y., Zaman, S.B., Lee, C.S., Jeong, Y., 2018. A crystal plasticity model for describing the anisotropic hardening behavior of steel sheets during strain-path changes. Int. J. Plast. 111, 85–106.

Kim, J.H., Kim, D., Barlat, F., Lee, M.-G., 2012. Crystal plasticity approach for predicting the Bauschinger effect in dual-phase steels. Mater. Sci. Eng. A 539, 259–270.

Kraska, M., Doig, M., Tikhomirov, D., Raabe, D., Roters, F., 2009. Virtual material testing for stamping simulations based on polycrystal plasticity. Comput. Mater. Sci. 46 (2), 383–392.

Kuwabara, T., Sugawara, F., 2013. Multiaxial tube expansion test method for measurement of sheet metal deformation behavior under biaxial tension for a large strain range. Int. J. Plast. 45, 103–118.

Lee, S.-Y., Kim, J.-H., Barlat, F., 2023. Appropriateness of hydrostatic pressure-based modeling for strength differential effect in advanced high strength steel. Mech. Mater. 186, 104807.

Li, S., Guo, C., Hao, L., Kang, Y., An, Y., 2019. In-situ EBSD study of deformation behaviour of 600 MPa grade dual phase steel during uniaxial tensile tests. Mater. Sci. Eng. A 759, 624–632.

Li, Q., Zhang, H., Chen, F., Xu, D., Sui, D., Cui, Z., 2020. Study on the plastic anisotropy of advanced high strength steel sheet: Experiments and microstructure-based crystal plasticity modeling. Int. J. Mech. Sci. 176, 105569.

Liao, J., Xue, X., Lee, M.-G., Barlat, F., Vincze, G., Pereira, A.B., 2017. Constitutive modeling for path-dependent behavior and its influence on twist springback. Int. J. Plast. 93, 64–88.

Liu, W., 2021. A multi-scale modelling framework for anisotropy prediction in aluminium alloy sheet and its application in the optimisation of the deep-drawing process. Int. J. Adv. Manuf. Technol. 17.

Liu, W., Chen, B.K., Pang, Y., 2019a. Numerical investigation of evolution of earing, anisotropic yield and plastic potentials in cold rolled FCC aluminium alloy based on the crystallographic texture measurements. Eur. J. Mech. A Solids 75, 41–55.

Liu, W., Chen, B.K., Pang, Y., Najafzadeh, A., 2020a. A 3D phenomenological yield function with both in and out-of-plane mechanical anisotropy using full-field crystal plasticity spectral method for modelling sheet metal forming of strong textured aluminum alloy. Int. J. Solids Struct. 193–194, 117–133.

Liu, Y., Fan, D., Bhat, S.P., Srivastava, A., 2020b. Ductile fracture of dual-phase steel sheets under bending. Int. J. Plast. 125, 80–96.

Liu, W., Huang, J., Liu, J., Wu, X., Zhang, K., Huang, A., 2021. Experimental and crystal plasticity modelling study on the crack initiation in micro-texture regions of Ti-6Al-4V during high cycle fatigue tests. Int. J. Fatigue 106203.

Liu, W., Huang, J., Pang, Y., Zhu, K., Li, S., Ma, J., 2023. Multi-scale modelling of evolving plastic anisotropy during Al-alloy sheet forming. Int. J. Mech. Sci. 247, 108168.

Liu, W., Lian, J., Aravas, N., Münstermann, S., 2020c. A strategy for synthetic microstructure generation and crystal plasticity parameter calibration of fine-grain-structured dual-phase steel. Int. J. Plast. 126, 102614.

Liu, X., Xue, Q., Wang, W., Zhou, L., Jiang, P., Ma, H., Yuan, F., Wei, Y., Wu, X., 2019b. Back-stress-induced strengthening and strain hardening in dual-phase steel. Materialia 7, 100376.

Ma, H., Li, Y., Zhang, H., Li, Q., Chen, F., Cui, Z., 2022. A virtual laboratory based on full-field crystal plasticity simulation to characterize the multiscale mechanical properties of AHSS. Sci. Rep. 12 (1), 5054.

Marcadet, S.J., Mohr, D., 2015. Effect of compression–tension loading reversal on the strain to fracture of dual phase steel sheets. Int. J. Plast. 72, 21–43.

Marie, A., Toros, H., Aksen, A., Alves, J.L., Amaral, R.L., Betaieb, E., Chandola, N., 2022. Analysis of ESAFORM 2021 cup drawing benchmark of an Al alloy , critical factors for accuracy and efficiency of FE simulations. Int. J. Mater. Form. 15, 61.

Min, J., Guo, N., Hou, Y., Jiang, K., Chen, X., Carsley, J.E., Lin, J., 2021. Effect of tension-compression testing strategy on kinematic model calibration and springback simulation of advanced high strength steels. Int. J. Mater. Form. 14 (3), 435–448.

Park, S., Jung, J., Cho, W., Jeong, B.-S., Na, H., Kim, S.-I., Lee, M.-G., Han, H.N., 2021. Predictive dual-scale finite element simulation for hole expansion failure of ferrite-bainite steel. Int. J. Plast. 136, 102900.

Poulin, C.M., Korkolis, Y.P., Kinsey, B.L., Knezevic, M., 2019. Over five-times improved elongation-to-fracture of dual-phase 1180 steel by continuous-bending-under-tension. Mater. Des. 161, 95–105.

Quey, R., Dawson, P., Barbe, F., 2011. Large-scale 3D random polycrystals for the finite element method: Generation, meshing and remeshing. Comput. Methods Appl. Mech. Engrg. 200 (17–20), 1729–1745.

Ravi, S.K., Seefeldt, M., Van Bael, A., Gawad, J., Roose, D., 2019. Multi-scale material modelling to predict the material anisotropy of multi-phase steels. Comput. Mater. Sci. 160, 382–396.

Roters, F., Diehl, M., Shanthraj, P., Eisenlohr, P., Reuber, C., Wong, S., Maiti, T., Ebrahimi, A., Hochrainer, T., Fabritius, H.-O., Nikolov, S., Friák, M., Fujita, N., Grilli, N., Janssens, K., Jia, N., Kok, P., Ma, D., Meier, F., Werner, E., Stricker, M., Weygand, D., Raabe, D., 2019. DAMASK – The Düsseldorf Advanced Material Simulation Kit for modeling multi-physics crystal plasticity, thermal, and damage phenomena from the single crystal up to the component scale. Comput. Mater. Sci. 158, 420–478.

Roters, F., Eisenlohr, P., Hantcherli, L., Tjahjanto, D., Bieler, T., Raabe, D., 2010. Overview of constitutive laws, kinematics, homogenization and multiscale methods in crystal plasticity finite-element modeling: Theory, experiments, applications. Acta Mater. 58 (4), 1152–1211.

Shanthraj, P., Eisenlohr, P., Diehl, M., Roters, F., 2015. Numerically robust spectral methods for crystal plasticity simulations of heterogeneous materials. Int. J. Plast. 66, 31–45.

Shi, S., Li, Y., Yan, Z., Yang, S., Ju, Y., 2022. Crystal plasticity phase-field simulation of slip system anisotropy during creep of Co-Al-V monocrystal alloy under multidirectional strain. Int. J. Mech. Sci. 227, 107436.

Soliman, M., Palkowski, H., 2020. Tensile properties and bake hardening response of dual phase steels with varied martensite volume fraction. Mater. Sci. Eng. A 777, 139044.

Tang, X., Wang, Z., Wang, X., Deng, L., Zhang, M., Gong, P., Jin, J., Fu, M., 2023. Unraveling size-affected plastic heterogeneity and asymmetry during micro-scaled deformation of CP-Ti by non-local crystal plasticity modeling. Int. J. Plast. 170, 103733.

Tasan, C., Diehl, M., Yan, D., Zambaldi, C., Shanthraj, P., Roters, F., Raabe, D., 2014. Integrated experimental–simulation analysis of stress and strain partitioning in multiphase alloys. Acta Mater. 81, 386–400.

Tian, C., Ponge, D., Christiansen, L., Kirchlechner, C., 2020. On the mechanical heterogeneity in dual phase steel grades: Activation of slip systems and deformation of martensite in DP800. Acta Mater. 183, 274–284.

Wagoner, R.H., Lim, H., Lee, M.-G., 2013. Advanced Issues in springback. Int. J. Plast. 45, 3–20, In Honor of Rob Wagoner.

Welo, T., Ringen, G., Ma, J., 2020. An overview and evaluation of alternative forming processes for complex aluminium products. Procedia Manuf. 48 (2019), 82–89.

Wollmershauser, J., Clausen, B., Agnew, S., 2012. A slip system-based kinematic hardening model application to in situ neutron diffraction of cyclic deformation of austenitic stainless steel. Int. J. Fatigue 36 (1), 181–193.

Xu, Z., Zhang, R., Peng, L., Fu, M., 2023. Crystal plasticity-based analysis and modelling of grain size and strain path dependent micro-scaled deformation mechanisms of ultra-thin sheet metals. Int. J. Plast. 168, 103696.

Xue, X., Liao, J., Vincze, G., Barlat, F., 2017. Twist springback characteristics of dual-phase steel sheet after non-axisymmetric deep drawing. Int. J. Mater. Form. 10 (2), 267–278.

Xue, X., Liao, J., Vincze, G., Pereira, A.B., Barlat, F., 2016a. Experimental assessment of nonlinear elastic behaviour of dual-phase steels and application to springback prediction. Int. J. Mech. Sci. 117, 1–15.

Xue, X., Liao, J., Vincze, G., Sousa, J., Barlat, F., Gracio, J., 2016b. Modelling and sensitivity analysis of twist springback in deep drawing of dual-phase steel. Mater. Des. 90, 204–217.

Yalçinkaya, T., Çakmak, S.O., Tekoğlu, C., 2021. A crystal plasticity based finite element framework for RVE calculations of two-phase materials: Void nucleation in dual-phase steels. Finite Elem. Anal. Des. 187, 103510.

Yang, H., Li, H., Sun, H., Zhang, Y., Liu, X., Zhan, M., Liu, Y., Fu, M., 2022. Anisotropic plasticity and fracture of alpha titanium sheets from cryogenic to warm temperatures. Int. J. Plast. 156, 103348.

Yoshida, F., Hamasaki, H., Uemori, T., 2015. Modeling of anisotropic hardening of sheet metals including description of the Bauschinger effect. Int. J. Plast. 75, 170–188.

Yoshida, F., Uemori, T., 2002. A model of large-strain cyclic plasticity describing the Bauschinger effect and workhardening stagnation. Int. J. Plast. 18 (5–6), 661–686.

Yoshida, F., Uemori, T., 2003. A model of large-strain cyclic plasticity and its application to springback simulation. Int. J. Mech. Sci. 45 (10), 1687–1702.

Yoshida, F., Uemori, T., Fujiwara, K., 2002. Elastic–plastic behavior of steel sheets under in-plane cyclic tension–compression at large strain. Int. J. Plast. 18 (5–6), 633–659.

Zecevic, M., Korkolis, Y.P., Kuwabara, T., Knezevic, M., 2016. Dual-phase steel sheets under cyclic tension–compression to large strains: Experiments and crystal plasticity modeling. J. Mech. Phys. Solids 96, 65–87.

Zhang, H., Diehl, M., Roters, F., Raabe, D., 2016. A virtual laboratory using high resolution crystal plasticity simulations to determine the initial yield surface for sheet metal forming operations. Int. J. Plast. 80, 111–138.

Zhang, K., Holmedal, B., Hopperstad, O., Dumoulin, S., Gawad, J., Van Bael, A., Van Houtte, P., 2015. Multi-level modelling of mechanical anisotropy of commercial pure aluminium plate: Crystal plasticity models, advanced yield functions and parameter identification. Int. J. Plast. 66, 3–30.

Zhang, W., Xu, J., 2022. Advanced lightweight materials for Automobiles: A review. Mater. Des. 110994.